Journal of
Materials Chemistry B

Materials for biology and medicine

rsc.li/materials-b
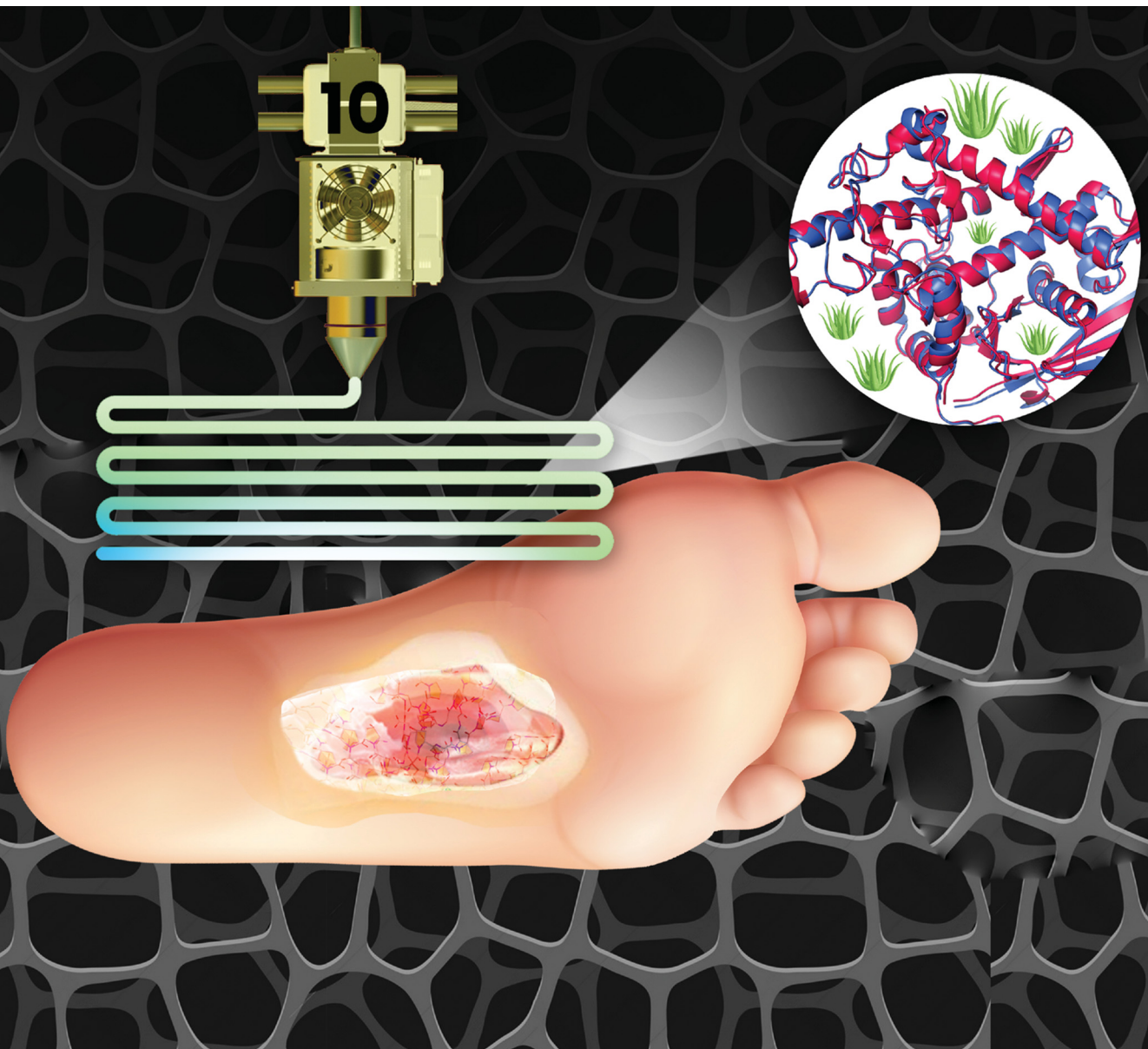
PAPER
Anita Kamra Verma, Shilpi Chaudhary,
Avanish Singh Parmar *et al*.
3D printable, injectable amyloid-based composite hydrogel
of bovine serum albumin and aloe vera for rapid diabetic
wound healing

ROYAL SOCIETY
OF CHEMISTRY

10 YEARS
ANNIVERSARY

3D printable, injectable amyloid-based composite hydrogel of bovine serum albumin and aloe vera for rapid diabetic wound healing†

Kaustubh Naik,[a] Priyanka Singh,‡[b] Monika Yadav,‡[b] Saurabh Kr Srivastava,‡[a] Shikha Tripathi,[a] Rahul Ranjan,[c] Prodyut Dhar,[c] Anita Kamra Verma,*[b] Shilpi Chaudhary*[d] and Avanish Singh Parmar [ID] *[ae]

Protein-based biomaterials, particularly amyloids, have sparked considerable scientific interest in recent years due to their exceptional mechanical strength, excellent biocompatibility and bioactivity. In this work, we have synthesized a novel amyloid-based composite hydrogel consisting of bovine serum albumin (BSA) and aloe vera (AV) gel to utilize the medicinal properties of the AV gel and circumvent its mechanical frangibility. The synthesized composite hydrogel demonstrated an excellent porous structure, self-fluorescence, non-toxicity, and controlled rheological properties. Moreover, this hydrogel possesses inherent antioxidant and antibacterial properties, which accelerate the rapid healing of wounds. The *in vitro* wound healing capabilities of the synthesized composite hydrogel were evaluated using 3T3 fibroblast cells. Moreover, the efficacy of the hydrogel in accelerating chronic wound healing *via* collagen crosslinking was investigated through *in vivo* experiments using a diabetic mouse skin model. The findings indicate that the composite hydrogel, when applied, promotes wound healing by inducing collagen deposition and upregulating the expression of vascular endothelial growth factor (VEGF) and its receptors. We also demonstrate the feasibility of the 3D printing of the BSA–AV hydrogel, which can be tailored to treat various types of wound. The 3D printed hydrogel exhibits excellent shape fidelity and mechanical properties that can be utilized for personalized treatment and rapid chronic wound healing. Taken together, the BSA–AV hydrogel has great potential as a bio-ink in tissue engineering as a dermal substitute for customizable skin regeneration.

1. Introduction

Having achieved significant accomplishments in academic research and commercialization over the past decade, hydrogels have emerged as a captivating feature of modern materials science.[1,2] Researchers and engineers have been captivated by the distinct and varied attributes exhibited by these hydrogels, which offer immense potential for numerous interesting applications. Composed of a three-dimensional network of water-soluble polymers, hydrogels can absorb and retain large amounts of water. This class of biomaterials possess exceptional and fascinating properties, such as a highly porous structure, a high water content, controlled biodegradability, tuneable mechanical and rheological properties, and low immunogenicity. In the past decade, hydrogels have garnered significant interest owing to their excellent properties for use in a wide range of biomedical applications, including tissue engineering,[3,4] drug delivery,[5,6] wound dressing,[7,8] artificial organs,[9,10] regenerative medicine,[11,12] and wearable sensors.[13,14] In recent years, naturally occurring hydrogels, which are made from biomolecules or derived from medicinal plants, have received considerable interest for biomedical purposes owing to their inherent medicinal properties, non-toxicity, and diverse functionalities.[15] Aloe vera (AV) is a hydrogel that has been utilized widely by humans for centuries due to its numerous therapeutic effects, such as wound healing, anti-inflammatory, anti-bacterial, anti-aging, and antiseptic properties.[16–18] The AV hydrogel contains almost 95% water along with 75 potentially

[a] *Biophysics and Nanotechnology Laboratory, Department of Physics, Indian Institute of Technology (BHU), Varanasi, Uttar Pradesh 221005, India. E-mail: asparmar.phy@itbhu.ac.in*

[b] *Nanobiotech Lab, Kirorimal College, University of Delhi, 110007, Delhi, India. E-mail: akverma@kmc.du.ac.in*

[c] *School of Biochemical Engineering, Indian Institute of Technology (BHU), Varanasi, Uttar Pradesh 221005, India*

[d] *Department of Applied Sciences, Punjab Engineering College (Deemed to be University), Chandigarh, 160012, India. E-mail: shilpichaudhary@pec.edu.in*

[e] *Centre for Biomaterials and Tissue Engineering, Indian Institute of Technology (BHU), Varanasi, India*

† Electronic supplementary information (ESI) available: Experimental section, diabetes wound model treatment, and histopathological studies. See DOI: https://doi.org/10.1039/d3tb01151h

‡ Equal contribution.

8142 | *J. Mater. Chem. B*, 2023, 11, 8142–8158

This journal is © The Royal Society of Chemistry 2023

bioactive compounds, including lipids, amino acids, enzymes, polysaccharides, vitamins, and minerals.[19] For example, AV gel contains polysaccharides, notably acemannan, which possess a remarkable ability to bind to cell membranes and plasma proteins.[20] This characteristic facilitates the acceleration of wound healing by augmenting the production of collagen.[21] Furthermore, polysaccharides stimulate fibroblasts to produce vital components for restoration of the extracellular matrix, namely hyaluronic acid and hydroxyproline.[22] In addition, barbaloin and other polyphenolic compounds act as antioxidants to inhibit free-radical-mediated cytotoxicity and lipid peroxidation, to provide firmness and hydration to the skin.[23] Despite having diverse and countless medicinal benefits, the poor mechanical strength of AV gel constrains its utilization in biomedical applications.[24] Different strategies have been reported to increase the mechanical strength of AV hydrogels, through reinforcement with a stiffer material that has a tuneable mechanical strength, such as alginate,[25] chitosan,[26] cellulose,[24,27] gelatine,[26] or collagen.[28]

By contrast, globular proteins have a propensity to self-assemble into amyloid fibrils, which have been implicated in a number of neurodegenerative diseases *in vivo*.[29] These amyloid fibrils are widely recognized to be the stiffest biological material, with a mechanical strength comparable to steel.[30,31] Amyloid fibrils are a good candidate for nanobiotechnological applications because they tend to form hydrogels with excellent stability and tuneable mechanical characteristics under specific physicochemical conditions.[32] Such amyloid-based hydrogels possess remarkable biocompatibility and controlled biodegradability due to their highly ordered structure and the multifunctional moieties of the protein molecule.[32] Recently, researchers have demonstrated the *in vitro* formation of amyloid fibril-based hydrogels using diverse proteins such as bovine serum albumin (BSA),[33] lysozyme,[34] lactoglobulin,[35] *etc.* In particular, BSA has received a lot of attention due to its low cost and biocompatibility. BSA is a 66 kDa protein that is derived from cow serum, and it comprises a single polypeptide chain of 583 amino acids and has 17 cysteine residues.[36,37] In addition, the cysteine residues of BSA use self-assembled disulfide linkages to form a cross-linked stable hydrogel under certain conditions, such as a change in the pH or temperature, or the addition of a cross-linking agent.

Herein, a novel and composite hydrogel has been developed by integrating AV into BSA under various concentrations. The aim was to improve the diverse physical properties of aloe vera hydrogels and optimize their efficacy in facilitating wound healing. To the best of our knowledge, this is the first instance of creating a printable hydrogel that incorporates AV gel into the amyloid-based protein BSA. The proposed hydrogel was thoroughly investigated to determine its physical and chemical properties, revealing its highly porous structure, excellent UV absorption, bright
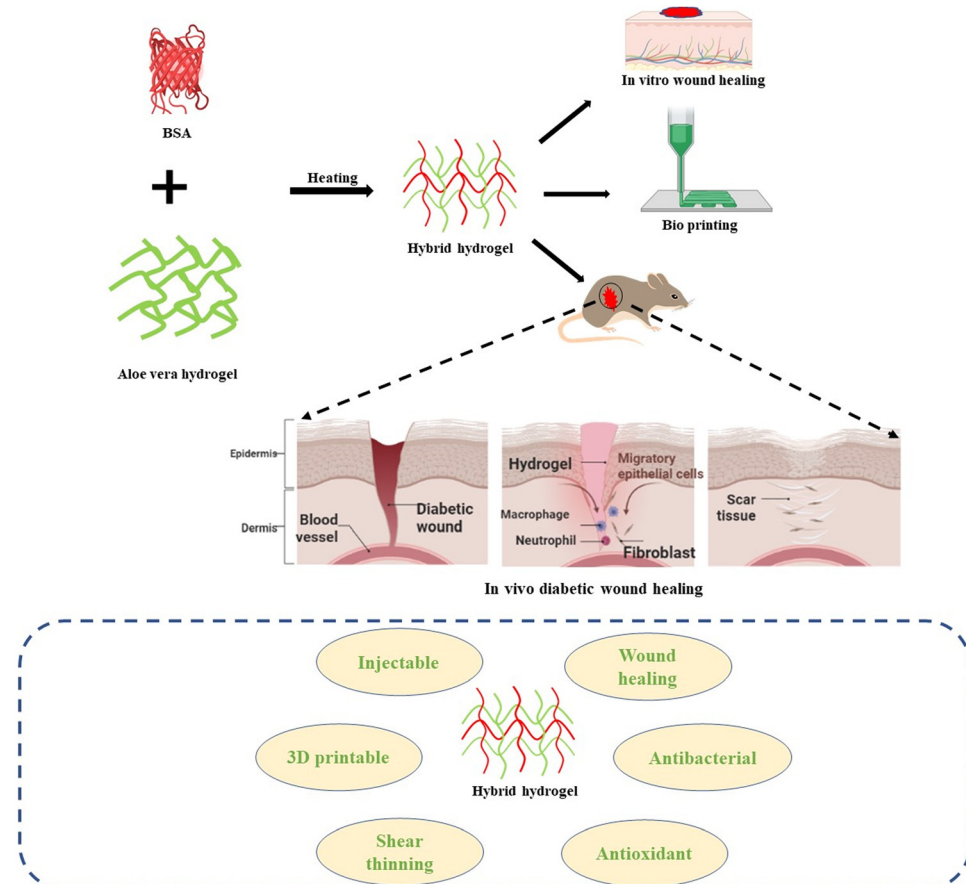
Scheme 1 Schematic for the synthesis of the composite hydrogel from BSA and AV for chronic wound healing.

This journal is © The Royal Society of Chemistry 2023

J. Mater. Chem. B, 2023, **11**, 8142–8158 | **8143**

fluorescence, and adjustable rheological properties. As shown in Scheme 1, both *in vitro* and *in vivo* testing of the composite hydrogel revealed an accelerated chronic wound healing efficacy. Furthermore, we developed a stable 3D printed geometry with a high shape fidelity for tailored wound dressing applications.

2. Experimental section

2.1 Materials

BSA (lyophilized powder, 96%), hydrochloric acid, sodium chloride, sodium dihydrogen phosphate, and sodium hydroxide disodium hydrogen phosphate were purchased from Sigma-Aldrich. Spray-dried AV gel powder 200X (*Aloe barbadensis*) was received from Heilen Biopharm, Gandhinagar, India. Ultrapure water (12 MΩ cm), produced by a Millipore water purification system, was used for the preparation of aqueous solutions throughout all of the experimental work. All chemicals were of analytical grade and were used without further purification.

2.2 Synthesis of hydrogels

Aqueous solutions of BSA (80 mg mL^{-1}) were formed by dissolving lyophilized BSA powder in PBS buffer. Furthermore, different amounts (% (w/v)) of AV gel powder were added to the BSA solution and stirred gently to form homogenous solutions. All of the solutions were prepared in a glass beaker and then transferred to glass vials for further reaction. The prepared solutions were heated at 70 °C until they passed the vial inversion test (for 30–45 minutes) to obtain a hydrogel. During heating, for the different concentrations of AV powder in BSA solution, hydrogels of different rheological properties are formed. The prepared hydrogels were prepared at a fixed BSA concentration of 80 mg mL^{-1} with various concentrations of AV, and they are labelled as AxB8, where x = 8, 6, 4, 2, and 0% (w/v) of AV gel powder in a fixed concentration of BSA solution (80 mg mL^{-1}).

2.3 Characterization

Characterization of the hydrogels was performed to determine their physiochemical properties. The precursor solution of the hydrogel was used to determine the zeta potential. After the formation of the hydrogel, the rheological and mechanical behaviour was investigated. After that, these hydrogels were lyophilized to determine their morphology, UV absorption, photoluminescence, degradation (*via* FTIR studies), swelling behaviour, and thermal properties. The detailed experimental procedures are discussed in the ESI.†

2.4 Fabrication of 3D printed structures

A customized extrusion printer from Alfatek Systems (India) was used to fabricate the 3D printed dressings. The composite hydrogel was loaded into a syringe (Alfatek Systems) with a 22-gauge (410 μm) needle size. The syringe was then loaded on to the extruder of the 3D bioprinter. Structures of dimensions 3 × 3 × 0.5 cm (20 layers) were printed using Mendel software at a printing speed of 5 mm min^{-1}. The printed structures were freeze dried overnight before further characterization.

2.5 Antioxidant and antibacterial activities

To assess the antioxidant capability of the hydrogels, a 2,2-diphenyl-1-picrylhydrazyl (DPPH) radical scavenging activity test and a cellular oxidative damage model were used, based on a previously published method.[38] More information on the methods can be found in the ESI.†

For evaluating the antibacterial properties of each hydrogel, *Escherichia coli* (*E. coli*) and *Staphylococcus aureus* (*S. aureus*) were used in agar diffusion and spread plate assays. The ESI† provides detailed information on the methods used.

2.6 *In vitro* studies

The biocompatibility, percentage viability and wound healing capability of the hydrogels were evaluated and calculated using the Swiss mouse embryonic tissue, NIH-3T3 cell line. In addition to that, the hemolytic activity of the hydrogels was assessed with human blood cells. The selected regions of interest for the cells were analysed using a Nikon inverted microscope on a 10× objective at 0 h and 24 h to determine the scratch area, percentage wound coverage, and average and standard deviation of the scratch width using the ImageJ software. The detailed experimental procedure is described in the ESI.†

2.7 *In vivo* wound healing examination

Diabetes was induced in rats with a single dose of streptozotocin (STZ) (60 mg kg^{-1} body weight, *via* intraperitoneal injection in 0.1 M citrate buffer, pH 4.5), and subsequent blood glucose levels were monitored using a gluco-meter *via* the tail vain. After the 8th day a wound was made on the back of the animal, which was a full-thickness open-excision wound made using a biopsy puncture, the area of which was also disinfected with 70% ethanol. After wound induction, the diabetic animals were randomly divided into five groups as follows: group 1 (normal control); group 2 (diabetes wound control); group 3 (A0B8 treated diabetes wound); group 4 (A8B0 treated diabetes wound); and group 5 (A6B8 treated diabetes wound). Treatment was provided *via* the topical administration of the synthesized formulation (A8B0, A0B8 or A6B8 hydrogel) on an alternate basis over the subsequent 21 days. The blood glucose and body weight were routinely measured. At the end of the experiment the animals underwent fasting overnight and were then sacrificed. Serum samples were isolated and kept frozen at −80 °C until biochemical analysis was carried out. Other organs and wound tissue were also isolated for estimation of the oxidative stress biomarkers and related histopathological studies. All of the experimental procedures were performed according to the approved guidelines from the Institutional Animal Ethics Committee, Kirori Mal College, University of Delhi, New Delhi (Registration no. 1666/GO/Re/S/12/CPCSEA, Protocol no. DU/KR/IAEC/2023/15B) for care and use in laboratory.

The detailed experimental procedure has been described in the ESI.†

3. Results and discussion

The composite BSA–AV hydrogel was obtained by heating the precursor solutions above the melting temperature of BSA

8144 | *J. Mater. Chem. B*, 2023, **11**, 8142–8158

This journal is © The Royal Society of Chemistry 2023

(70 °C). The solution was heated until it formed a translucent gel that passed the vial inversion test in the shortest possible time.[39] All of the preheated solutions showed a high negative zeta potential, as depicted in Fig. 1A and B. The zeta potential values indicate the presence of high surface charges on the protein, giving an excellent dispersion stability and preventing the aggregation of BSA due to electrostatic repulsion. The gel formation was confirmed using the vial inversion test, as depicted in Fig. 1B. Initially, the solution is in a liquid form, which transforms into a jiggly gel, and finally turns into a soft gel. These hydrogels were lyophilized at −80 °C for 24 h and stored at 4 °C for subsequent analysis. The synthesized hydrogels were characterized to investigate their various physical and chemical properties. It was observed from vial inversion test that the gelation time increased with an increased concentration of the AV gel. The increase in the concentration of the AV gel can lead to a reduction in the intermolecular interactions between the BSA molecules, resulting in a slower

formation of the hydrogel. BSA is well known to undergo concentration-dependent gelation when heated near to or above its melting temperature at a pH away from its isoelectric point.[40] This phenomenon is initiated by the partial unfolding of BSA, resulting in weakening of the hydrogen bonds within the monomer due to thermal fluctuations and thus exposing hydrophobic residues, resulting in an aggregation process that depends on the interaction equilibrium between hydrophobic and electrostatic interactions.[41–43]

3.1 Morphology and porosity

The surface morphology and porosity of the hydrogels were observed *via* SEM of the lyophilized samples, as depicted in Fig. 1C. All composite hydrogels exhibit highly porous structures with several micron-sized voids. Interestingly, as shown in Table 1, as the concentration of the AV gel is increased, the composite hydrogels exhibit a uniform honeycomb-like three-dimensional supramolecular assembly due to their ability to
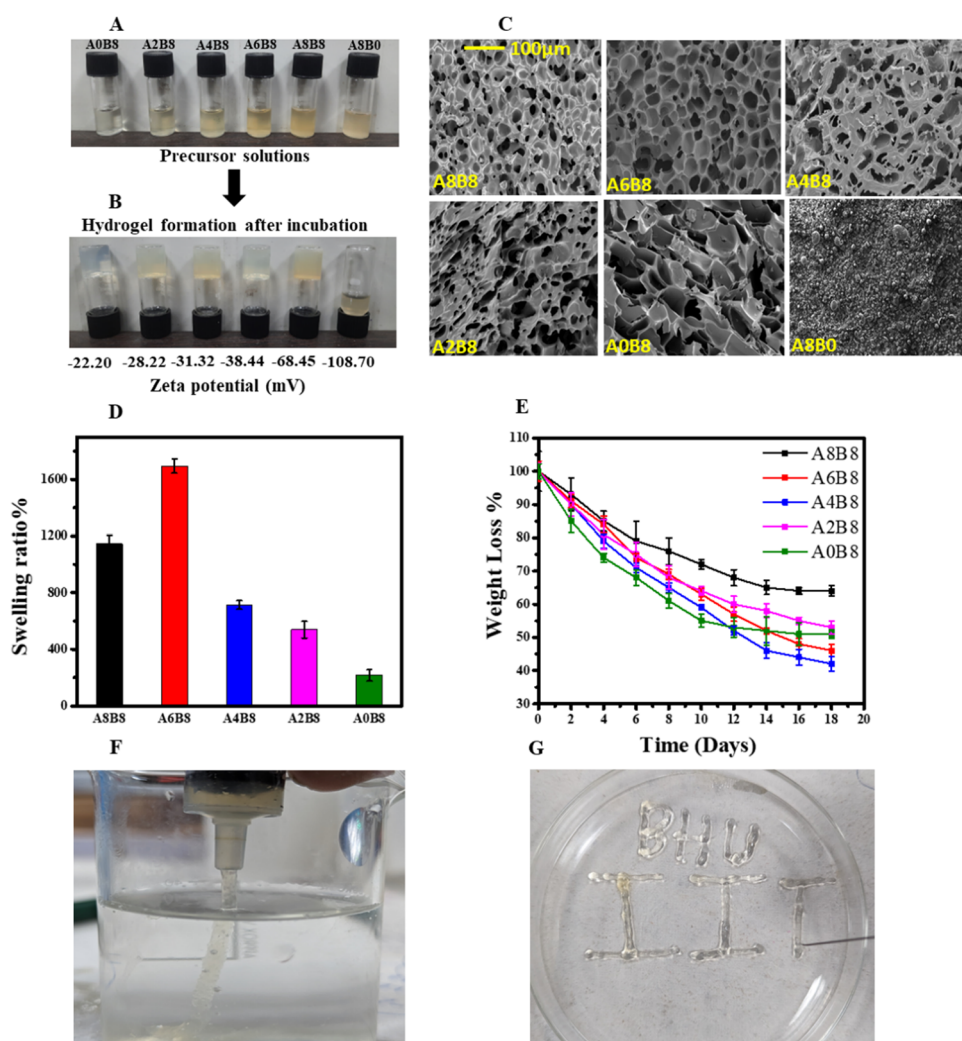
Fig. 1 Vial inversion test and microscopic images of the hydrogels. (A) Preheated precursor solutions. (B) Illustration of the vial inversion test for various compositions of the BSA and AV hydrogels, with zeta potential values shown for each gel. (C) SEM images of the hydrogels showing highly porous structures. (D) Swelling ratios of the hydrogels after 24 h. (E) Weight loss study of the hydrogels. (F and G) Injectable behavior of the A6B8 hydrogel in water *via* a syringe.

This journal is © The Royal Society of Chemistry 2023

J. Mater. Chem. B, 2023, **11**, 8142–8158 | **8145**

Table 1 Representing average area (μm^2), standard deviation (μm^2), and average length (μm) of hydrogel porosity

Sample	Average area (μm^2)	Standard deviation (μm^2)	Average length (μm)
A8B8	25.97	3.65	55.00
A6B8	29.23	2.66	60.43
A4B8	24.66	13.39	53.66
A2B8	16.12	12.22	34.32
A0B8	39.33	14.86	84.04

form hydrogen bond networks with BSA. It is observed from the SEM images that A8B8 shows an overexpression of AV, leading to a reduced degree of porosity in its morphology. Consequently, it is postulated that A6B8 represents a more advantageous candidate, with its optimized and well-organized porosity standing out as a notable attribute. The pore size and interconnectivity of a hydrogel can be adjusted through the modification of its AV content. This enables the synthesis of porous hydrogels with tunable structures. Moreover, it is hypothesized that, since the BSA is heated slightly below its melting temperature, its secondary structure, or beta sheet formation, is still present. Consequently, weaker and fewer intermolecular physical bonds form between the partially denatured BSA molecules, which induces re-solubilization of the gel when it is cooled to room temperature.[39] The exact gelation temperature of the composite hydrogels was determined *via* a rheometer temperature sweep (Fig. 2A).

The swelling of the lyophilized hydrogel was examined to investigate the capability of hydrogel dehydration for transportation/storage and prior-to-use rehydration as a wound dressing. It was observed that the composite hydrogels show a relatively high swelling ratio with a gradual increase with the concentration of AV gel (monitored after 24 h) up to an optimum content, as depicted in Fig. 1D. The control A0B8 hydrogel revealed a degree of swelling of 210% after 24 h. As expected, the swelling ratio of the composite hydrogels increased, reaching 1750% when the AV gel content was 6% (w/v) (A6B8), before it decreased with a further increase in the AV content for A8B8. The high swelling ratio for the composite hydrogels is attributed to the hydrophilic compounds present in AV and BSA, which effectively absorbed water molecules. It can be further hypothesized that the high swelling ratio of the composite hydrogels is due to uniform and interconnected voids which provide adequate free volume to accumulate the water entering the hydrogels. Thus, this trend in the swelling ratio is in good agreement with the SEM images and rheological observations. The weight loss study of hydrogels is crucial for the wound healing process. If the hydrogel degrades too quickly, it may not provide adequate support for the wound and may impede the healing process. Conversely, if the hydrogel degrades too slowly, it may prolong the healing time, leading to complications such as infection. Therefore, understanding the weight loss behaviour of hydrogels is essential in developing effective wound healing materials. Fig. 1E describes the weight loss of all the hydrogels examined over a period of 18 days. All hydrogels showed significant weight loss due to a well cross-linked polymer network. However, hydrogels with a higher BSA content exhibited significant weight loss, which is attributable to the double-cross-linked network of the protein, which includes hydrogen bonds, beta-sheet crystalline domains, hydrophobic groups, and a highly crystalline structure, leading to the hydrogel undergoing rapid degradation. In addition, there will be significant cleavage between hydrogen bonds and hydrophobic bonds, which causes decomposition of the hydrogel network. The injection process for the A6B8 hydrogel is illustrated in Fig. 1(F and G), showing that it can be extruded smoothly from a 19 G needle with an inner diameter of 0.5 mm without any blockages. This hydrogel ink is able to be successfully dispensed through a syringe and can be used to fill moulds of various shapes. In the cases of irregular or deep wounds, this hydrogel wound dressing can be conveniently injected into the wound area, adhering well to the wound, and conforming to its shape.

3.2 Rheological analysis

Temperature ramp experiments were performed to determine the gelation temperature and phase changes of the different solutions. To evaluate this, G' and G'' were plotted as a function of the temperature at a constant frequency of 10 rad s^{-1} and a constant strain of 1% (Fig. 2A). Initially, at a low temperature (below 70 °C), the loss modulus (G'') was dominant due to the low viscosity. With a further increase in the temperature, there is a sharp increase in the storage modulus (G') due to formation of the gel at that temperature.[44] As observed, the gelation temperature was found to be between 70 and 80 °C for all of the different hydrogel compositions. From Fig. 2A it can be seen that the gelation temperature increases with the AV concentration, indicating late-onset gelation, which is further supported by the vial inversion test results (Fig. 1A).

To fabricate the required structure, the rheological properties of the hydrogels play a vital role in 3D extrusion. For extrusion-based 3D printing, hydrogels must possess shear thinning behaviour. This behaviour is characterized by a change in the viscosity as the shear rate is increased. As shown in Fig. 2B, the smooth curves reveal that the hydrogels show excellent shear thinning behaviour, indicating the formation of uniformly cross-linked hydrogels.[45] Under shear, superstructures are broken down into their aggregates, resulting in the formation of an immobilized hydrogel network, which is free to move with increasing shear rate.[45,46] Interestingly, all hydrogels show similar shear thinning behaviour when the shear rate is increased from 0.1 to 100 s^{-1}.

The viscoelastic properties were further evaluated by performing amplitude and frequency sweep tests. The amplitude sweep was performed to determine the yield stress and deformation behaviour or linear viscoelastic range (LVR) in the non-destructive deformation range at a constant frequency of 1 rad s^{-1}, as shown in Fig. 2C.[47] In the LVR, the storage modulus G' and the loss modulus G'' are independent of the applied shear strain and hence the curve of G' is used to determine the limiting value or linearity limit of the LVR in terms of strain as a percentage.[48] The limiting value was determined at the point where the G' suddenly decreased. For A0B8, G' changed
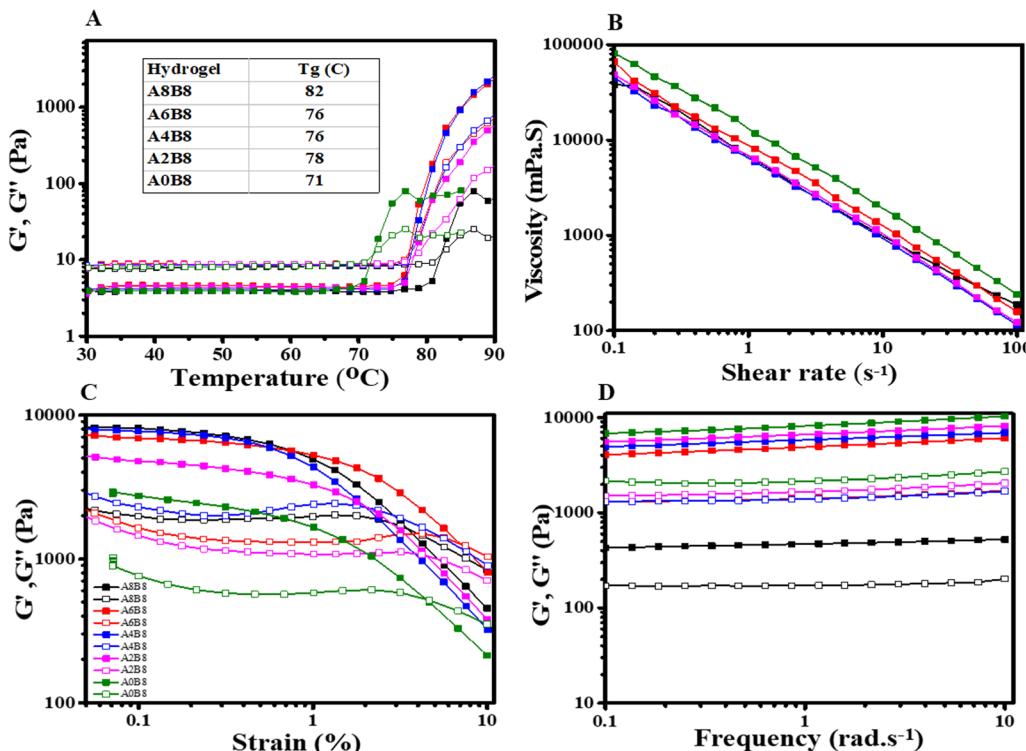
Fig. 2 Rheological characterization of the hydrogels. (A) Temperature sweep for each hydrogel, illustrating the gelation temperature (T_g) as the cross-point between G' and G'', where the inset lists the gelation temperature of each hydrogel. (B) Viscosity curve showing shear the thinning behaviour of the hydrogels. (C) Amplitude sweep at a constant frequency of 1 rad s^{-1}. (D) Frequency sweep at a constant shear strain of 1%. Throughout, the green symbols represent A0B8, pink symbols represent A2B8, blue symbols represent A4B8, red symbols represent A6B8 and black symbols represent A8B8; the filled and unfilled symbols denote G' and G'', respectively.

significantly at 1% strain, a linearity limit of strain, whereas this plateau region increased with the addition of the AV gel due to the formation of a consistent, three-dimensional cross-linked network. Furthermore, all hydrogels revealed a gradual decrease in modulus or breakdown with an increase in strain. This explains the injectable and smooth texture of the hydrogels. In addition, all hydrogels revealed predominant elastic behaviour at a low shear rate ($G' > G''$) then dynamic yield stress ($G' = G''$) and a viscous nature ($G'' > G'$) at a higher shear rate.

In addition, a frequency sweep in the LVR region was also performed to describe the structure and viscoelastic nature of the hydrogels, as depicted in Fig. 2D. For the frequency sweep, a constant strain of 1% was applied and G' and G'' were plotted as a function of the frequency. As can be seen from Fig. 2D, all gels show $G' > G''$ over the given frequency range, indicating their predominantly elastic nature and stability over long-term storage due to a stable network of forces.[49] In addition, both G' and G'' are nearly constant and independent across the entire frequency range from 0.1 to 10 rad s^{-1}.

3.3 Chemical and thermal characterization

The gelation mechanism was investigated using UV-Vis spectroscopy. It has been well reported that the UV-Vis spectrum of a BSA solution (unheated) shows a typical characteristic peak at 279 nm, which is caused by the aromatic amino acids tyrosine, tryptophan, and phenylaniline.[50] When the BSA solution is

heated near its melting temperature, it begins to aggregate, and eventually forms a gel. The pure BSA hydrogel (A0B8) shows this characteristic BSA peak in addition to another peak at 216 nm (Fig. 3A). The broad absorption around 279 nm suggests that the hydrophobic tyrosine residue becomes more exposed while the tryptophan residue is covered more due to the hydrophobic microenvironment during the formation of the gel.[39] By contrast, the pure AV gel (A8B0) shows multiple absorption peaks at 352 nm (UV A region), 294 nm (UV B region), and 269 nm (UV C region), as shown in Fig. 3A. The presence of carbonyl groups and phenolic compounds in AV accounts for the wide absorption peak observed at 352 nm.[51] It has been well reported that the typical UV absorption observed in this phyto-extract arises due to the existence of conjugated double bonds that are present in phenolic compounds of phyto-origin.[22] Interestingly, the composite hydrogels of AV–BSA, A8B8 and A6B8 in particular, exhibit a wide absorption over the entire UV range, suggesting the possibility of the generation of multiple new fluorescent moieties on the surface during the gelation process.

The photoluminescence of the composite hydrogels was studied and compared with the pure AV hydrogel and the control BSA hydrogel. Fig. 3B depicts the fluorescence spectra using an excitation wavelength of 360 nm. All of the hydrogels exhibited blue broad autofluorescence. The origin of the bright and wide range fluorescence is still unknown; however, certain
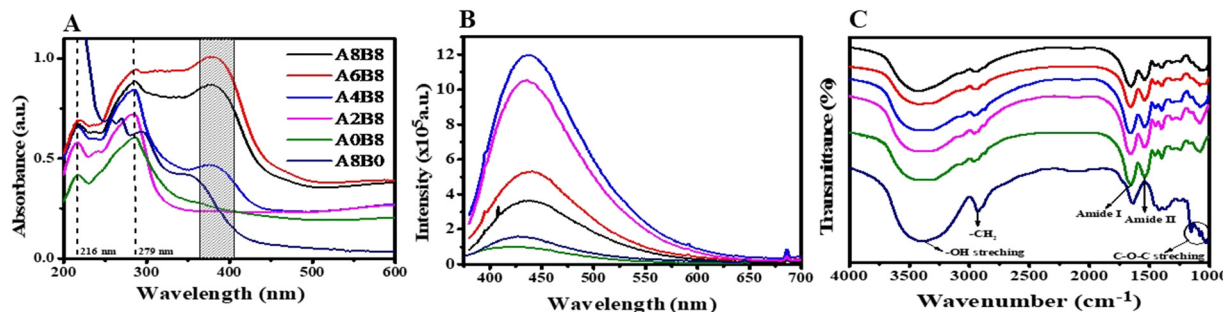
Fig. 3 Optical characterization of the lyophilized hydrogels. (A) UV-Vis absorbance spectra, (B) photoluminescence spectra, and (C) FTIR spectra, confirming the presence of the protein backbone, *i.e.*, amide bonds.

assumptions have been proposed, such as the quantum confinement effect, surface states, and molecule states.[52,53] The bright fluorescence observed for the pure AV gel can be attributed to the presence of numerous oxygen-containing functional groups and various aromatic compounds. By contrast, the control A0B8 hydrogel revealed fluorescence with a broad emission between 400 and 550 nm. This is assigned to a reduction in the steric hindrance of peptide chains and excessive exposure to the aromatic amino acids such as Tyr, Trp, and Phe, which may induce energy transfer among the C=C and C=O bonds present in BSA.[50] In addition, the broad emission suggests that new fluorophores are formed during the thermally induced gelation process. In the composite hydrogels, self-quenching fluorescence was observed at higher concentrations of AV. The exact mechanism of this phenomenon is still under debate; however, processes such as electron transfer, energy transfer, and the formation of new complex compounds may be responsible for this self-quenching fluorescence.[54–56]

FTIR spectroscopy was performed to identify the chemical bonding and functional groups present in the hydrogels of different compositions. All of the samples (BSA, AV, and the composite hydrogels) show a broad and intense peak at 3500 cm^{-1}, due mainly to OH stretching vibration modes, as depicted in Fig. 3C. Since the N–H stretching of amino acids is superimposed on the OH stretching vibration bands, a thorough analysis cannot be performed in this region. Pure AV (A8B0) exhibited several distinct spectral features. These include a sharp peak at 2920 cm^{-1}, which corresponds to the stretching of aliphatic –CH$_2$. In addition, a broad peak at 1470–1350 cm^{-1} was observed, which was assigned to non-symmetric –CH$_2$ scissoring and bending. Another notable feature was the sharp peak at 1650 cm^{-1}, which was attributed to C–O stretching. The presence of polysaccharide sugars, such as mannose and glucose, was also indicated by the bands observed around 1260–1000 cm^{-1}, which corresponded to the C–O–C glycosidic symmetric stretching vibrations of acetylated polysaccharides, indicating the presence of polysaccharide sugars such as mannose and glucose.[21] These results are consistent with a number of previously reported studies.[57] By contrast, the FTIR spectrum of A0B8 (pure BSA) revealed the presence of the fingerprint amide band region at 1520 cm^{-1} and 1650 cm^{-1} confirming that the inherent backbone chain of the protein remains intact

throughout the gelation process. For the composite hydrogels, all of the characteristic peaks of A0B8 were also present.[58] Notably, the peaks due to C–O stretching (1650 cm^{-1}) and CH$_2$ stretching (2920 cm^{-1}) are reduced in the composite hydrogel. It may possible that the interaction between the AV gel and BSA occurs *via* the formation of H bonds. Furthermore, the –OH group, –NH$_2$ group, and the –C=O group in the AV gel may form hydrogen bonds with the –OH and –NH$_2$ groups of BSA. Moreover, a polyanionic–polycationic complex could be formed through the creation of ionic interactions between the positively charged molecules of AV and the negatively charged residues of BSA. However, based on the FTIR results, it is not possible to comment on the formation of new complexes between AV and BSA due to their similar functional groups.

The thermal degradation behaviour and the stability of the hydrogels were analysed using thermogravimetric analysis (TGA), as shown in Fig. 4B. The pure AV gel and the composite hydrogels show degradation and weight loss at different temperatures, indicating that some chemical changes occur in the composite hydrogels when they are heated. For instance, the pure AV gel (A8B0) shows the first weight loss in the temperature range from 80 to 150 °C due to the loss of physically adsorbed water molecules. The second mass loss is due to thermal polymer degradation starting at about 210 °C. The final weight loss occurs between 400 and 700 °C due to the carbonization of the material. By contrast, the composites and the pure BSA hydrogel behave in the same way, but with a significant shift in the second weight loss temperature (250 °C) due to protein degradation at high temperature. This suggests that the hydrophilic properties were improved with better thermal stability.

3.4 Mechanical strength

Mechanical properties such as stability and elasticity are required for wound dressing hydrogels, and these were evaluated using a compression test. As shown in Fig. 4A, all of the composite hydrogels exhibited excellent stability and their maintained structural integrity during the compression test. In addition, all of the composite hydrogels revealed soft and stretchable behaviour, indicating a high degree of crosslinking due to the large amount of water trapped in the hydrogel pores. The compression modulus changed significantly after the
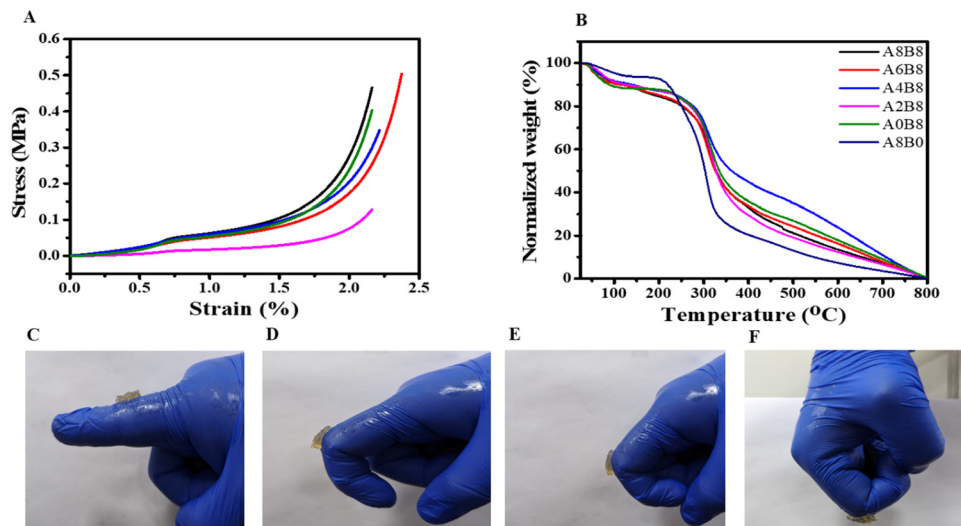
Fig. 4 (A) Compression stress–strain curves of the hydrogels. (B) TGA thermograms of the lyophilized hydrogels. (C–F) Images of A6B8 applied to the finger joint at different angles.

addition of AV, specifically at higher concentration, suggesting the formation of a robust and strong matrix due to the formation of large numbers of hydrogen bonds with AV. In summary, the composite hydrogels demonstrated a compatible compression modulus that matches the requirements and is consistent with what has been reported previously for wound healing and tissue engineering applications.[24,54,59] Furthermore, it was observed that the hydrogel adhered firmly to the fingers, maintaining its position even when the fingers were bent at angles ranging from 0 to 90°, as depicted in Fig. 4(C–F). This strong adhesion can be attributed to the robust hydrogen bonding that occurs between the hydrogel and the fingers.

3.5 Fabrication and study of a 3D printed scaffold

For an optimal outcome from the 3D printing of hydrogels, careful attention must be paid to two key factors: shape fidelity and integrity.[60,61] It is observed that, for the bioprinting of hydrogels, the extrusion method offers unique benefits which include versatility, high-throughput printing, controlled resolution, and accessibility compared with other methods. Fig. 5A shows that the mesh structure was successfully printed using the A6B8 hydrogel, demonstrating the potential of this material for producing a high shape fidelity. One of the key advantages of the A6B8 hydrogel is its excellent porous morphology and high swelling ratio. This implies that the material flows more easily under the printing conditions, and thickens again after its extrusion from the nozzle. In addition, the A6B8 hydrogel has a lower yield stress than the applied stress on the nozzle tip. This means that it is less likely to clog the nozzle or spread out excessively during printing. These properties enable the hydrogel to be printed with good accuracy and fair resolution using a 22 G needle. Another important consideration for the 3D printing of hydrogels is the possibility of distortion or collapse during or after the printing process. However, each layer of the printed structure using the A6B8 hydrogel remained intact
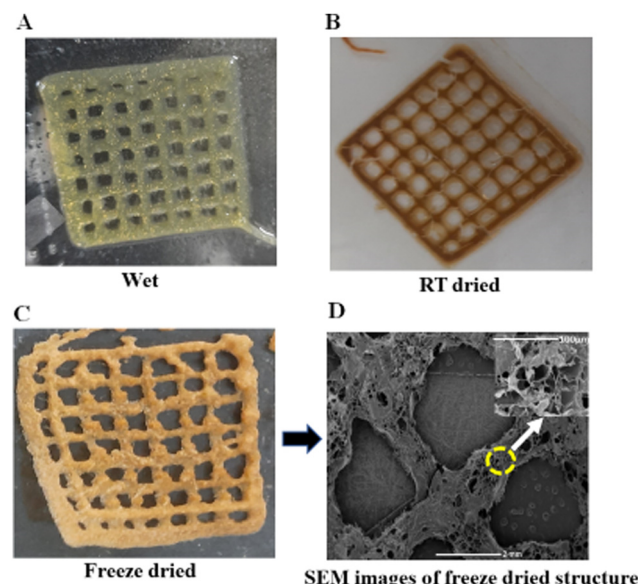

Fig. 5 3D printed structure of the A6B8 hydrogel: (A) freshly constructed wet sample; (B) lyophilized sample; (C) sample dried at room temperature; and (D) SEM image of 3D printed lyophilized hydrogel structure, where the inset shows a magnified image of the are highlighted with the yellow circle.

and self-supporting throughout the printing process, with no sign of collapse or distortion. This is due to the material's exceptional self-supporting properties. Fig. 5B and C show that the printed structures can be dried in two ways: freeze-drying and room-temperature drying. The freeze-dried samples maintained their shape more effectively and uniformly compared with the samples dried at room temperature, which showed small cracks that are probably due to the trapped water content. This suggests that freeze-drying is a more effective way to preserve the shape fidelity and integrity of the printed structures.

This journal is © The Royal Society of Chemistry 2023

J. Mater. Chem. B, 2023, **11**, 8142–8158 | **8149**

The SEM image presented in Fig. 5D illustrates the excellent structural integrity and high porosity of the freeze-dried A6B8 hydrogel sample. This porous nature is a highly desirable trait for certain applications, such as tissue engineering and drug delivery, as it enables the exchange of nutrients and other substances between the hydrogel and its surroundings. These findings demonstrate the potential of the A6B8 hydrogel for successful 3D printing with good shape fidelity and integrity. Furthermore, the unique properties of this hydrogel, such as its self-supporting and shear-thinning behaviour, make it a promising candidate for a wide range of 3D printing applications, including those in the biomedical and industrial sectors.

3.6 Antioxidant and antibacterial properties

Antioxidants have been shown to provide numerous health benefits by preventing oxidative stress, which can impede the repair and regeneration of tissue.[62] In diabetes-related diseases, hyperglycemia exacerbates oxidative stress by damaging enzymes and cellular machinery, as well as increasing insulin resistance.[63] Thus, a composite hydrogel with ROS-scavenging activities may be useful in treating diabetes. Composite BSA–AV hydrogels are a promising option for this purpose, as the antioxidant properties of AV have been well-studied, and its excellent radical-scavenging effects are attributed to its *ortho*-hydroxyl groups, which not only provide antioxidant properties by forming intramolecular hydrogen bonds but also stabilize the formed antioxidant radical.[64]

The present study examined the antioxidant activities of the composite hydrogels by assessing their ability to scavenge free radicals (*i.e.*, 2,2-diphenyl-1-picrylhydrazyl (DPPH), and hydroxyl (OH$^\bullet$)) as well as their total reducing power. DPPH is a free radical that reacts with antioxidants as a hydrogen receptor, and decolorization of the DPPH radical solution from purple (with a strong absorption at 517 nm) to colorless was used to measure the antioxidant activities of the hydrogels *via* the DPPH assay. As the concentration of AV was increased (from A2B8 to A8B8), the composite hydrogel showed a more significant DPPH scavenging effect than A0B8 (Fig. 6A). However, we observed that the DPPH scavenging effect of the hydrogels decreased with an increase in the H_2O_2 concentration, which is probably due to the higher H_2O_2 concentration that reduced the pore size of the hydrogel matrices, thereby decreasing the diffusion rate of DPPH into the hydrogels. For example, the A8B8 hydrogel exhibited a DPPH scavenging effect of approximately 92%, whereas the scavenging effect of the A6B8 and A4B8 hydrogels decreased to approximately 60% and 50%, respectively (Fig. 6B).

For the antibacterial properties of the composite hydrogel, an ideal wound dressing should possess antibacterial properties to safeguard the wound against external bacteria, limit the spread of microorganisms at the wound site, and mitigate inflammation. In this research, we used *S. aureus* and *E. coli* to assess the surface antibacterial potential of the hydrogels. After a 24 h incubation period at 37 °C, the composite hydrogels killed more than 50% of *S. aureus* and *E. coli* cells, indicating
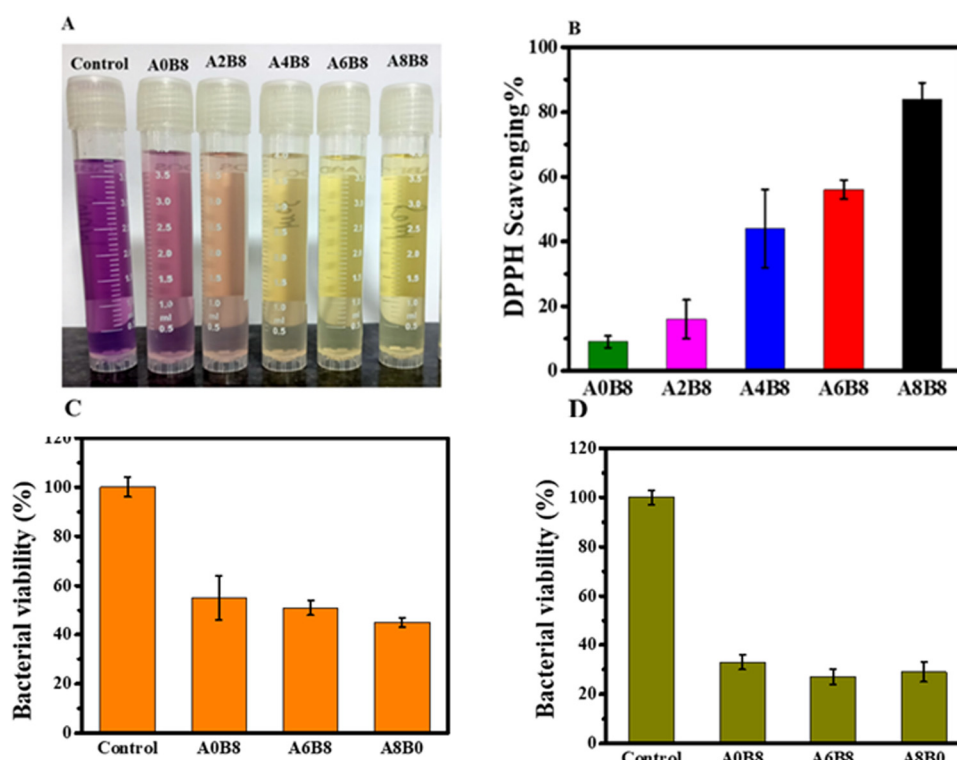
Fig. 6 (A) Change in absorbance of DPPH when exposed to the hydrogels with an increase in H_2O_2 concentration. (B) DPPH scavenging activity with the hydrogels. (C and D) Percentage bacterial viability of *S. aureus* (C) and *E. coli* (D) when exposed to the hydrogel samples.

their effectiveness in inhibiting bacterial propagation. However, the A8B8 hydrogel caused cell death in over 65% of cells, whereas the A6B8 and A4B8 hydrogels killed only 52% and 50% of the cells, respectively, as indicated in Fig. 6(C and D). The inhibition zone reflects a reduction in the bacterial colony population in that region. Consequently, we conclude that all composite hydrogels (BSA–AV) possess antibacterial activity.

3.7 *In vitro* biocompatibility and wound healing assay

Biocompatibility is a necessary requirement for the development of any compound intended for biomedical applications. In this study, the biocompatibility of the hydrogels was evaluated using the MTT colorimetric assay to assess the percentage cell viability. This assay involves the conversion of MTT to purple-colored formazan crystals by mitochondrial dehydrogenase in live cells. NIH-3T3 cells were cultured in the presence of increasing concentrations of hydrogels (1, 2, 4 and 8 mg mL^{-1}) for 24 h, 48 h, and 72 h, and the cell viability was measured. A dose- and time-dependent decrease in the cell viability was observed for the A8B8, A6B8, A4B8, and A2B8 hydrogels. This decrease was more pronounced at the concentration of 8 mg mL^{-1}, where a decrease of approximately

25–30% occurred after 72 h. However, the results showed that none of the concentrations used in the study were toxic to the NIH-3T3 fibroblast cells, and even at the highest concentration of 8 mg mL^{-1}, where the cell viability was approximately 72–76% after 24 h. The slight differences in cell viability at each time point were attributed to the concentration of the agent used during their synthesis. The results of this study, as shown in Fig. 7A, suggest that the prepared hydrogels are biocompatible with fibroblasts and could be a promising material for biomedical applications such as drug delivery and wound healing. To further evaluate the biocompatibility of the hydrogels, a hemolysis assay was conducted. This assay is considered to be a simple and reliable method for assessing the biocompatibility of materials. The results (Fig. 7B) showed that the hydrogels at concentrations of both 1 and 5 mg mL^{-1} exhibited very low hemolytic activity compared with the positive control after 2 h, 4 h, and 6 h. The hemolytic performance of the hydrogels was verified with the positive control Triton X-100 and the negative control phosphate buffer saline (PBS). The interaction of the hydrogels with red blood cells (RBCs) showed a hemolysis percentage of less than 5%, the critical safe hemolytic ratio for biomaterials according to ISO/TR 7406, indicating
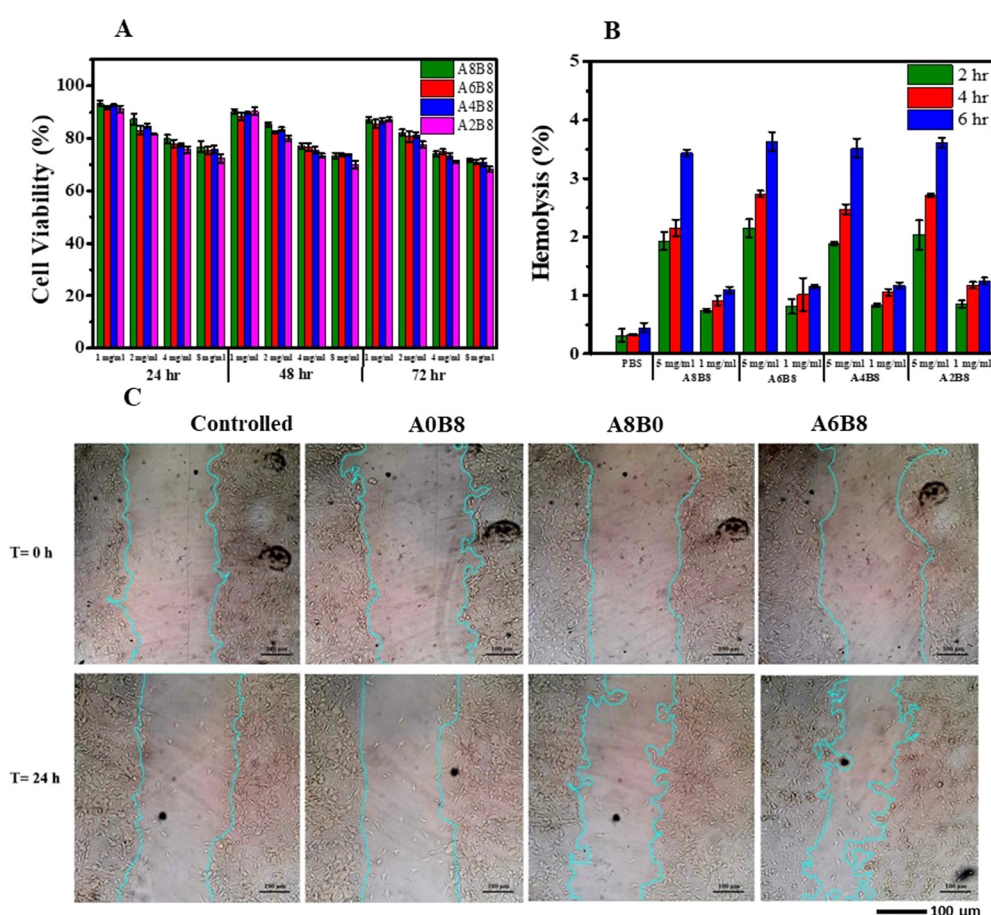

Fig. 7 *In vitro* characterization of the hydrogels. (A) Percentage viability on the NIH-3T3 cell line after 24, 48 and 72 h. (B) *Ex vivo* hemolysis of hydrogels with RBCs after 2 h (green), 4 h (red) and 6 h (blue). (C) Time lapse images (for 0 and 24 h) of wound healing closure in the NIH-3T3 cells exposed to the hydrogels.

This journal is © The Royal Society of Chemistry 2023

J. Mater. Chem. B, 2023, **11**, 8142–8158 | **8151**

that the damage to the RBCs by the hydrogels was minimal, even after 8 h of incubation time at both concentrations used during the study. In conclusion, the results of this study indicate that the investigated hydrogels are biocompatible and can be a potential candidate for biomedical applications. The MTT assay and hemolysis assay showed that the hydrogels did not show any significant toxicity to the cells or RBCs, respectively. These findings suggest that further *in vivo* studies could be conducted to explore the efficacy of these hydrogels in biomedical applications.

In this study, we investigated the effect of the hydrogel-containing medium on wound healing using an *in vitro* cell model. Our findings, as depicted in Fig. 7C, demonstrated that the hydrogel promoted wound healing. We observed a reduction in the scratch area of the wound after 24 hours of exposure to the hydrogel, as compared to the control group. Moreover, the width of the scratch was also decreased after 24 hours in the presence of the hydrogel. The standard deviation of the scratch width was analyzed to understand the heterogeneity of the scratch width at each time point, and the results suggested differences in the migration patterns of the cells. Interestingly, the deviation of the width did not appear to

be influenced by the evaluation time or the type of medium used. Our results also showed that the rate of cell migration increased after exposure to the hydrogel, and it approached an average value of 4.21 μm h^{-1} after 24 hours until the end of the experiment. These findings suggest that the hydrogel-containing medium may have potential applications in promoting wound healing.

3.8 *In vivo* study

Wound healing is delayed in diabetes mellitus individuals due to the chronic hyperglycaemic condition.[63] The functional wound healing properties of herbal phytochemicals could be a strategic approach for progressive wound healing for the diabetes condition.[65] In this context, our study aimed at better healing through the topical application of hydrogels, which is very new compared with the conventional approach. For this, an *in vivo* study was performed to assess the chronic wound healing potential of hydrogels prepared from BSA, AV and a combination of the two (A6B8), carried out using the chronic diabetic wound model as depicted in Fig. 8A in Wistar rats with diabetes induced using streptozotocin (STZ).[66] The administration of STZ for inducing diabetes mellitus is a widely used
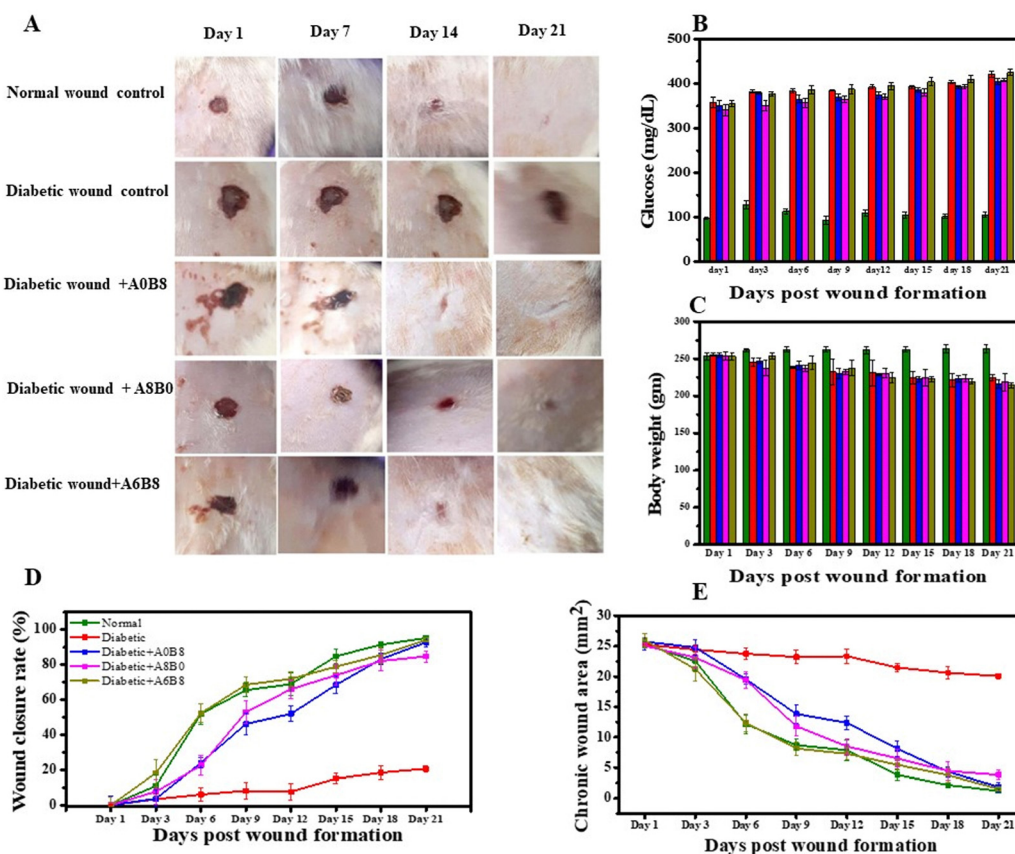
Fig. 8 (A) Representative photographs for the macroscopic assessment of wound healing for 5 groups (normal, diabetic control, diabetic + A0B8, diabetic + A8B0, diabetic + A6B8) recorded on Days 1, 7, 14 and 21 post wound formation. (B) Effect on blood glucose level for the control and treated groups post wound formation. (C) Effect on body weight for the control and treated groups post wound formation. (D) Effect of hydrogel treatment on the wound healing rate in the control and treated groups post wound formation. (E) Effect on the chronic wound area in the control and treated groups post wound formation. Color code for B–E: green, normal (non-diabetic); red, diabetic control; blue, diabetic + A0B8; pink, diabetic + A8B0; mustard, diabetic + A6B8.

8152 | *J. Mater. Chem. B*, 2023, **11**, 8142–8158

This journal is © The Royal Society of Chemistry 2023

method for assessing the healing properties of herbal-based hydrogels.[67] STZ is a diabetogenic agent that occurs naturally as an alkylating antineoplastic agent and is particularly hazardous to the insulin-producing beta cells of the pancreas in mammals. The glucose transporter is responsible for the uptake of STZ by pancreatic β-cells, resulting in cellular damage characterized by DNA fragmentation and apoptosis. Concurrently, the accumulation of reactive oxygen species, such as hydrogen peroxide, is observed, which further exacerbates the deterioration of cellular function. These pathological events culminate in impaired insulin production and glucose homeostasis, manifesting as hyperglycemia. The diabetes disease model was initially developed when the rats received a dose of STZ ranging from 50 to 65 mg kg^{-1} body weight.[68–70] The concentration of STZ and the route of administration determine the formation of the induced diabetes mellitus model. A diabetes mellitus model was utilized for validation purposes, and involved the measurement of glucose levels. Glucose levels exceeding 250 mg dL^{-1} were regarded as being indicative of diabetes mellitus. In addition, an excisional wound was created to facilitate studies related to diabetes-related wounds. The mean glucose level for all groups was represented in units of mg dL^{-1}; however, topical treatment of the wounds of diabetic rats with different hydrogel formulations did not result in any significant alteration in their blood glucose levels (Fig. 8B). The effect of STZ on the body weight of Wistar rats was also monitored, which was found to be reduced after the intraperitoneal administration of STZ. The mean body weight for all of the groups was represented in grams; however, a drop in body weight was observed in all of the diabetic rats, irrespective of the wound treatment using different hydrogel formulations, as shown in Fig. 8C. Moreover, excessive protein and lipid breakdown and/or dehydration may be linked to the body weight loss, as seen in diabetic rats.[70,71]

Throughout the experiment, regular macroscopic qualitative analysis was performed. On the first day of wound induction, all wounds were similar in appearance; however, significant differences in both the wound area and morphology were observed, as depicted in Fig. 8A. From days 7 to 21, distinct scar formation from the necrotic tissue residue was observed in various groups, along with noticeable clinical signs of inflammation, such as redness and swelling, which were alleviated by the topical application of the hydrogel formulation. Furthermore, re-epithelialization was observed, and the A6B8-treated group showed a faster rate of re-epithelialization compared with the diabetic control. Further wound healing was evaluated in terms of the chronic wound area and the wound closure rate. This revealed that the wounds in the 'diabetic wound + A6B8' group showed more rapid contraction compared with those in the normal control group (1.202 ± 0.299 mm^2; 95.241 ± 1.183%) and the diabetic control group (20.060 ± 0.417 mm^2; 20.645 ± 1.650%), with a wound closure area and a closure rate of 1.533 ± 0.310 mm^2; 94.091 ± 1.197% as shown in Fig. 8(D and E). For the groups 'diabetic wound + A0B8' and 'diabetic wound + A8B0', the values are 1.852 ± 0.743 mm^2; 92.801 ± 2.887% and 3.814 ± 0.804 mm^2; 84.778 ± 3.209%, respectively.

These results suggest enhanced healing for a combination of both BSA and AV in the hydrogel compared with the 'diabetic wound control' group.

The effect of STZ on physiological homeostasis was determined in terms of the cellular reactive oxygen species (ROS) generated, more specifically on how free radicals of oxygen and nitrogen, which are represented as ROS and reactive nitrogen species (RNS), respectively, affect the final healing mechanism, where the occurrence of oxidative stress complicates the healing process. STZ administration increases protein glycation, lipolysis, ketogenesis, *etc.*, and decreases the levels of antioxidant substrates such as glutathione (GSH), and nicotinamide adenine dinucleotide phosphate dependent coenzyme Q reductase (NaD(P)HCoQ). Furthermore, nitric oxide (NO) and lactate dehydrogenase (LDH) are biomarkers that indicate oxidative stress in diabetes. For NO synthase (NOS), there has been a special focus on 3 isoenzymes, *i.e.*, eNOS, iNOS and nNOS, which promote the generation of NO through catalysing the oxidation of L-arginine to L-citrulline in a nicotinamide adenine dinucleotide phosphate reduced form (NADPH) *via* an oxygen-dependent reaction. Studies have indicated that the role of eNOS is mainly as a marker for angiogenesis under diabetic wound conditions, while iNOS is mainly as an marker for NO production. Therefore, both eNOS and iNOS play an important role in the healing process.[72,73] It has been reported that STZ destroys pancreatic beta cells, leading to hyperglycemia-induced altered glucose transport, dysfunctional mitochondrial bioenergetics and an imbalance in the rate of oxygen utilization by respiratory chain complexes, thus being responsible for non-healing complications. Oxidative stress and the effect on NO production was measured by the values obtained *via* NO assays (Fig. 9A and Fig. S1, ESI†): for the 'diabetic wound + A0B8' group it is 1.085 ± 0.693 μM mg^{-1}, for the 'diabetic wound + A8B0' groups it is 2.061 ± 0.624 μM mg^{-1}, but for the 'diabetic wound + A6B8' group the concentration of NO increased to 2.433 ± 0.177 μM mg^{-1} with respect to the normal (9.296 ± 0.461 μM mg^{-1}) and diabetic control groups (1.085 ± 0.693 μM mg^{-1}) (Fig. 9B). Assays for LDH, as a cellular biomarker for compromised cell membrane integrity, were carried out and the results are shown in Fig. 9C and Fig. S2, ESI.† The value for the 'diabetic wound + A0B8' group is 86.127 ± 13.497 nM mg^{-1}, and for the 'diabetic wound + A8B0' group it is 64.403 ± 3.815 nM mg^{-1}, but for the 'diabetic wound + A6B8' group the LDH concentration increased to 75.771 ± 6.893 nM mg^{-1} compared with the normal (24.805 ± 0.342 nM mg^{-1}) and diabetic control groups (160.133 ± 20.578 nM mg^{-1}) (Fig. 9C).[74] However, ROS generation in tissues is regulated through the inhibition of electron transfer at complex I (by the inhibitor rotenone) that augments radical formation. The oxidative stress-related assays carried out so far show reduced levels of oxidative stress markers, which will promote the healing mechanism in wound tissue post wound formation upon application of the applied hydrogel formulation. Superoxide dismutase is another free radical scavenger enzyme that rapidly catalyzes the dismutation of superoxide anions (O_2^-) and thus acts as a first line antioxidant defence mechanism. In the case of superoxide

This journal is © The Royal Society of Chemistry 2023

J. Mater. Chem. B, 2023, **11**, 8142–8158 | **8153**
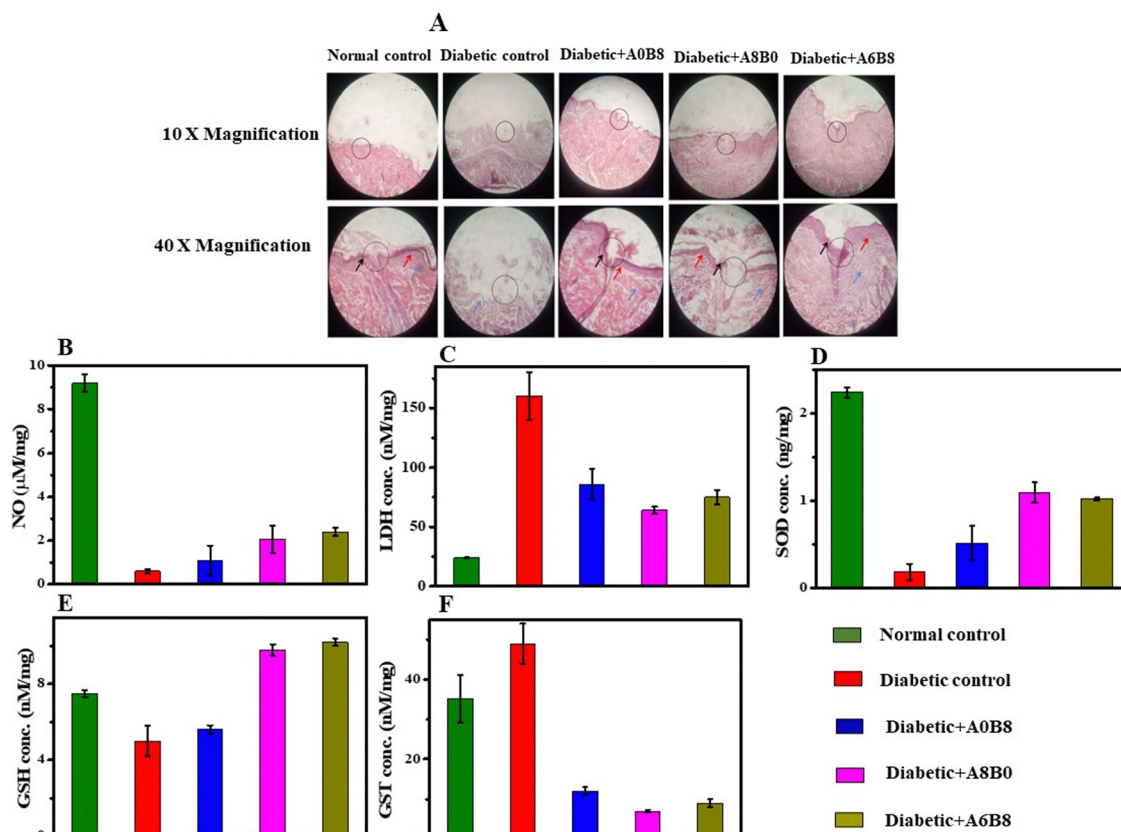
Fig. 9 (A) Histopathological anatomy of wound tissue: column 1 represents the normal (non-diabetic) control, column 2 represents the diabetic control, column 3 represents the diabetic wound + A0B8, column 4 represents the diabetic wound + A8B0, and column 5 represents the diabetic wound + A6B8; the top row presents images at 10× magnification, and the bottom row presents images at 40× magnification. The colored arrows denote the following: black, re-epithelialization; blue, collagen; red, fibrosis; the region marked with the black circle is the wound area. (B–F) Effect on NO concentration (B), LDH concentration (C), SOD concentration (D), GST concentration (E), and GSH concentration (F) on the wound tissue after hydrogel treatment in the control and treated groups. Color code for (B–F): green, normal (non-diabetic); red, diabetic control; blue, diabetic + A0B8; pink, diabetic + A8B0; mustard, diabetic + A6B8.

dismutase (SOD) deficiency, the superoxide anion reacts with NO to produce peroxynitrite ($ONOO^-$), which is a potent oxidant and nitrosating agent that can cause direct damage to proteins, lipids, and DNA. Under diabetic wound conditions, the concentration of the SOD enzyme in the 'diabetic wound + A6B8' group was 1.023 ± 0.015 ng mg^{-1} of the SOD enzyme present in the wound tissue, for the 'diabetic wound + A0B8' and 'diabetic wound + A8B0' groups the values are 0.517 ± 0.195 ng mg^{-1} and 1.098 ± 0.117 ng mg^{-1}; furthermore, these were compared with the normal control group and the diabetic control group, where the values were found to be 2.240 ± 0.058 ng mg^{-1} and 0.187 ± 0.094 ng mg^{-1}, respectively (Fig. 9D and Fig. S3, ESI†).[75] Concentration of GSH in the 'diabetic wound + A6B8' group was 10.199 ± 0.172 nM mg^{-1} compared with the normal control group (7.564 ± 0.180 nM mg^{-1}) and the diabetic control group (5.008 ± 0.838 nM mg^{-1}) (Fig. 9E and Fig. S4, ESI†). For the 'diabetic wound + A0B8' and 'diabetic wound + A8B0' groups the GSH concentrations are 5.635 ± 0.239 nM mg^{-1} and 9.810 ± 0.371 nM mg^{-1}, respectively[76] (Fig. 9E). Furthermore, the glutathione S-transferase (GST) concentration from the GST assay for the 'diabetic wound + A0B8'

group is 12.909 ± 1.388 nM mg^{-1} and for the 'diabetic wound + A8B0' group it is 7.532 ± 0.362 nM mg^{-1}, but for the 'diabetic wound + A6B8' group it increased to 9.302 ± 1.333 nM mg^{-1} with respect to the normal and diabetic control groups, at 35.191 ± 6.272 nM mg^{-1} and 49.959 ± 5.242 nM mg^{-1}, respectively (Fig. 9F and Fig. S5, ESI†). Thus, when the wound repair process is defective, stimulating collagen production will be advantageous for the potential healing of a chronic wound. These findings indicate that the administration of AV in conjunction with BSA via topical application stimulates collagen deposition and accelerates wound healing. This process is facilitated through the heightened expression of vascular endothelial growth factor (VEGF), an endogenous angiogenesis stimulant, and its receptors which are upregulated during wound healing. The upregulation of VEGF and its receptors increases the supply of oxygen and essential nutrients that are necessary for collagen synthesis at the chronic wound site. This finding suggests enhanced healing using a combination of both BSA and AV together in comparison with normal control wounds and diabetic wounds.

A histopathological examination was carried out via hematoxylin–eosin (H&E) staining 21 days after formation of the

wound tissue. This revealed epithelialization in normal control group and diabetic groups treated with the hydrogel, although no epithelialization was seen in the diabetic control group, as described in Fig. 9A. Furthermore, the orderly arrangement of the collagen content of granulation tissue in the diabetic control group was very low, probably confirming the presence of persistent inflammation and a high level of oxidative stress. Fibroblast proliferation under the epithelium also covered the wound area in the normal control group. However, there no inflammatory cells were seen. Although process of epithelialization was complete in the A6B8-treated group, fibroblast and collagen regeneration were also more evident in the A6B8-treated group, with properly arranged bundles sited parallel to the newly formed epidermis in comparison with the A0B8- and A8B0-treated groups.[77]

4. Conclusion

In this study, we developed a novel composite hydrogel by integrating the AV hydrogel with BSA at various concentrations. To our knowledge, this is the first instance of creating a printable hydrogel based on an AV–BSA composite. Our hydrogel offers unique advantages compared with existing solutions, such as additive-free formulation, 3D printability, and excellent rheological properties, making it highly promising for diverse biomedical applications. We found that the A6B8 sample is a more advantageous candidate, with its well-organized porosity, high swelling ratio and water uptake standing out as notable attributes. We conducted both *in vitro* and *in vivo* testing of the composite hydrogel, and the results showed an accelerated chronic wound healing efficacy. These results suggest that the topical application of the A6B8 hydrogel stimulated the deposition of collagen and thereby promoted wound healing through the increased expression of VEGF, leading to improved angiogenesis and the delivery of necessary nutrients for collagen synthesis. This finding suggests enhanced healing can be achieved using a hydrogel that contains both BSA and AV in comparison with normal control wounds and the diabetic wounds. Moreover, the 3D printability of our hydrogel enables the dressing to be customized to individual wounds, which makes it a promising option for personalized diabetic wound treatment. Overall, the BSA–AV hydrogel is shown to be a promising solution for personalized diabetic wound healing. Its unique combination of properties and the ability to customize the wound dressing to the specific needs of each patient makes it a valuable addition to the current wound healing options. However, further research is needed to evaluate the long-term effectiveness of this wound dressing in a clinical setting.

Author contributions

Kaustubh Naik: protocol design, synthesis, and characterization experiments, writing. Monica Yadav, Priyanka Singh: *in vitro* and *in vivo* experiment design and performance. Saurabh Kr Srivastava, Shikha Tripathi, Rahul Ranjan: experiment co-performance. Prodyut Dhar: instruction on 3D bioprinter instrument use. Anita Kamra Verma: *in vitro* and *in vivo* experiment design assistance and manuscript editing. Shilpi Chaudhary, Avanish Singh Parmar: project supervision, funding acquisition, research support, manuscript revision.

Conflicts of interest

The authors declare no competing financial interest.

Acknowledgements

References

1 C. Diaz and D. Missirlis, Amyloid-Based Albumin Hydrogels, *Adv. Healthc. Mater.*, 2023, **12**(7), 2201748, DOI: **10.1002/adhm.202201748**.

2 Y. S. Zhang and A. Khademhosseini, Advances in Engineering Hydrogels, *Science*, 2017, **356**, 6337, DOI: **10.1126/science.aaf3627**.

3 J. D. Tang, C. Mura and K. J. Lampe, Stimuli-Responsive, Pentapeptide, Nanofiber Hydrogel for Tissue Engineering, *J. Am. Chem. Soc.*, 2019, **141**(12), 4886–4899, DOI: **10.1021/jacs.8b13363**.

4 A. S. Hoffman, Hydrogels for Biomedical Applications, *Adv. Drug Deliv. Rev.*, 2012, **64**, 18–23, DOI: **10.1016/j.addr.2012.09.010**.

5 Y. Xiao, Y. Gu, L. Qin, L. Chen, X. Chen, W. Cui, F. Li, N. Xiang and X. He, Injectable Thermosensitive Hydrogel-Based Drug Delivery System for Local Cancer Therapy, *Colloids Surf., B*, 2021, **200**, 111581, DOI: **10.1016/j.colsurfb.2021.111581**.

6 Q. Chai, Y. Jiao and X. Yu, Hydrogels for Biomedical Applications: Their Characteristics and the Mechanisms behind Them, *Gels*, 2017, **3**(1), 6, DOI: **10.3390/gels3010006**.

7 S. H. Aswathy, U. Narendrakumar and I. Manjubala, Commercial Hydrogels for Biomedical Applications, *Heliyon*, 2020, **6**(4), e03719, DOI: **10.1016/j.heliyon.2020.e03719**.

8 Y. Liang, J. He and B. Guo, Functional Hydrogels as Wound Dressing to Enhance Wound Healing, *ACS Nano*, 2021, **15**(8), 12687–12722, DOI: **10.1021/acsnano.1c04206**.

9 D. Seliktar, Designing Cell-Compatible Hydrogels for Biomedical Applications, *Science*, 2012, **336**(6085), 1124–1128, DOI: **10.1126/science.1214804**.

10 Y. Wang, R. K. Kankala, C. Ou, A. Chen and Z. Yang, Advances in Hydrogel-Based Vascularized Tissues for Tissue Repair and Drug Screening, *Bioact. Mater.*, 2022, **9**, 198–220, DOI: **10.1016/j.bioactmat.2021.07.005**.

This journal is © The Royal Society of Chemistry 2023

J. Mater. Chem. B, 2023, **11**, 8142–8158 | 8155

11 M. C. Catoira, L. Fusaro, D. Di Francesco, M. Ramella and F. Boccafoschi, Overview of Natural Hydrogels for Regenerative Medicine Applications, *J. Mater. Sci. Mater. Med.*, 2019, **30**, 115, DOI: **10.1007/s10856-019-6318-7**.

12 A. K. Gaharwar, N. A. Peppas and A. Khademhosseini, Nanocomposite Hydrogels for Biomedical Applications, *Biotechnol. Bioeng.*, 2014, **111**(3), 441–453, DOI: **10.1002/bit.25160**.

13 L. Wang, T. Xu and X. Zhang, Multifunctional Conductive Hydrogel-Based Flexible Wearable Sensors, *TrAC - Trends Anal. Chem.*, 2021, **134**, 116130, DOI: **10.1016/j.trac.2020.116130**.

14 X. Sun, S. Agate, K. S. Salem, L. Lucia and L. Pal, Hydrogel-Based Sensor Networks: Compositions, Properties, and Applications—A Review, *ACS Appl. Bio Mater.*, 2021, **4**(1), 140–162, DOI: **10.1021/acsabm.0c01011**.

15 P. G. Kulkarni, N. Paudel, S. Magar, M. Fernanda and S. Shubham, Overcoming Challenges and Innovations in Orthopedic Prosthesis Design: An Interdisciplinary Perspective, *Biomed. Mater. Devices*, 2023, DOI: **10.1007/s44174-023-00087-8**.

16 W. Hanif, A. Hardiansyah, A. Randy and L. A. T. W. Asri, Physically Crosslinked PVA/Graphene-Based Materials/Aloe Vera Hydrogel with Antibacterial Activity, *RSC Adv.*, 2021, **11**(46), 29029–29041, DOI: **10.1039/d1ra04992e**.

17 A. Oryan, E. Alemzadeh, A. A. Mohammadi and A. Moshiri, Healing Potential of Injectable Aloe Vera Hydrogel Loaded by Adipose-Derived Stem Cell in Skin Tissue-Engineering in a Rat Burn Wound Model, *Cell Tissue Res.*, 2019, **377**(2), 215–227, DOI: **10.1007/s00441-019-03015-9**.

18 M. Saberian, E. Seyedjafari, S. J. Zargar, F. S. Mahdavi and P. Sanaei-rad, Fabrication and Characterization of Alginate/Chitosan Hydrogel Combined with Honey and Aloe Vera for Wound Dressing Applications, *J. Appl. Polym. Sci.*, 2021, **138**(47), 1–15, DOI: **10.1002/app.51398**.

19 S. Kumar, A. Yadav, M. Yadav and J. P. Yadav, Effect of Climate Change on Phytochemical Diversity, Total Phenolic Content and in Vitro Antioxidant Activity of Aloe Vera (L.) Burm. F, *BMC Res. Notes*, 2017, **10**(1), 60, DOI: **10.1186/s13104-017-2385-3**.

20 V. M. Rodríguez-González, A. Femenia, R. F. González-Laredo, N. E. Rocha-Guzmán, J. A. Gallegos-Infante, M. G. Candelas-Cadillo, P. Ramírez-Baca, S. Simal and C. Rosselló, Effects of Pasteurization on Bioactive Polysaccharide Acemannan and Cell Wall Polymers from Aloe Barbadensis Miller, *Carbohydr. Polym.*, 2011, **86**(4), 1675–1683, DOI: **10.1016/j.carbpol.2011.06.084**.

21 M. Ghorbani, P. Nezhad-Mokhtari and S. Ramazani, Aloe Vera-Loaded Nanofibrous Scaffold Based on Zein/Polycaprolactone/Collagen for Wound Healing, *Int. J. Biol. Macromol.*, 2020, **153**, 921–930, DOI: **10.1016/j.ijbiomac.2020.03.036**.

22 J. Hamman, Composition and Applications of Aloe Vera Leaf Gel, *Molecules*, 2008, **13**(8), 1599–1616, DOI: **10.3390/molecules13081599**.

23 J. Liang, L. Cui, J. Li, S. Guan, K. Zhang and J. Li, Aloe Vera: A Medicinal Plant Used in Skin Wound Healing, *Tissue Eng. Part B Rev.*, 2021, **27**(5), 455–474, DOI: **10.1089/ten.teb.2020.0236**.

24 H. Baniasadi, R. Ajdary, J. Trifol, O. J. Rojas and J. Sepp, Direct Ink Writing of Aloe Vera/Cellulose Nanofibrils Bio-Hydrogels, *Carbohydr. Polym.*, 2021, **266**, 118114, DOI: **10.1016/j.carbpol.2021.118114**.

25 A. Hadi, A. Nawab, F. Alam and K. Zehra, Sustainable Alginate/Aloe Vera Composite Biodegradable Films Reinforced with Carboxymethyl Cellulose and Hydroxypropyl Methylcellulose, *Polym. Compos.*, 2022, **43**(6), 3471–3480, DOI: **10.1002/pc.26629**.

26 D. E. López Angulo and P. J. do Amaral Sobral, Characterization of Gelatin/Chitosan Scaffold Blended with Aloe Vera and Snail Mucus for Biomedical Purpose, *Int. J. Biol. Macromol.*, 2016, **92**, 645–653, DOI: **10.1016/j.ijbiomac.2016.07.029**.

27 M. Ul-Islam, F. Ahmad, A. Fatima, N. Shah, S. Yasir, M. W. Ahmad, S. Manan and M. W. Ullah, Ex Situ Synthesis and Characterization of High Strength Multipurpose Bacterial Cellulose-Aloe Vera Hydrogels, *Front. Bioeng. Biotechnol.*, 2021, **9**, 601988, DOI: **10.3389/fbioe.2021.601988**.

28 P. Jithendra, A. M. Rajam, T. Kalaivani, A. B. Mandal and C. Rose, Preparation and Characterization of Aloe Vera Blended Collagen-Chitosan Composite Scaffold for Tissue Engineering Applications, *ACS Appl. Mater. Interfaces*, 2013, **5**(15), 7291–7298, DOI: **10.1021/am401637c**.

29 A. V. Maltsev, S. Bystryak and O. V. Galzitskaya, The Role of β-Amyloid Peptide in Neurodegenerative Diseases, *Ageing Res. Rev.*, 2011, **10**(4), 440–452, DOI: **10.1016/j.arr.2011.03.002**.

30 Z. Tang, H. He, L. Zhu, Z. Liu, J. Yang, G. Qin and J. Wu, A General Protein Unfolding-Chemical Coupling Strategy for Pure Protein Hydrogels with Mechanically Strong and Multifunctional Properties, *Adv. Sci.*, 2022, **9**(5), 2102557, DOI: **10.1002/advs.202102557**.

31 M. Schleeger, C. C. VandenAkker, T. Deckert-Gaudig, V. Deckert, K. P. Velikov, G. Koenderink and M. Bonn, Amyloids: From Molecular Structure to Mechanical Properties, *Polymer*, 2013, **54**(10), 2473–2488, DOI: **10.1016/j.polymer.2013.02.029**.

32 C. Diaz and D. Missirlis, Amyloid-Based Albumin Hydrogels, *Adv. Healthc. Mater.*, 2022, 2201748, DOI: **10.1002/adhm.202201748**.

33 K. Yadav, M. Das, N. K. Mishra, A. Chhabra, A. Mishra, S. Srivastava, P. Sharma, S. K. Yadav and A. S. Parmar, Tunning Self-Assembled Phases of Bovine Serum Albumin via Hydrothermal Process to Synthesize Novel Functional Hydrogel for Skin Protection against UVB, *Nanotechnol. Rev.*, 2022, 1643–1657.

34 T. Chen, Y. Wang, J. Xie, X. Qu and C. Liu, Lysozyme Amyloid Fibril-Integrated PEG Injectable Hydrogel Adhesive with Improved Antiswelling and Antibacterial Capabilities, *Biomacromolecules*, 2022, **23**(3), 1376–1391, DOI: **10.1021/acs.biomac.1c01597**.

35 J. Su, Y. Cai, Z. Zhi, Q. Guo, L. Mao, Y. Gao, F. Yuan and P. Van der Meeren, Assembly of Propylene Glycol Alginate/β-Lactoglobulin Composite Hydrogels Induced by Ethanol

for Co-Delivery of Probiotics and Curcumin, *Carbohydr. Polym.*, 2021, **254**, 117446, DOI: **10.1016/j.carbpol.2020.117446.**

36 K. Hirayama, S. Akashi, M. Furuya and K. Fukuhara, Rapid Confirmation and Revision of the Primary Structure of Bovine Serum Albumin by ESIMS and Frit-FAB LC/MS, *Biochem. Biophys. Res. Commun.*, 1990, **173**(2), 639–646, DOI: **10.1016/S0006-291X(05)80083-X.**

37 V. Bloomfield, The Structure of Bovine Serum Albumin at Low PH, *Biochemistry*, 1966, **5**(2), 684–689, DOI: **10.1021/bi00866a039**.

38 J. Ding, Y. Yao, J. Li, Y. Duan, J. R. Nakkala, X. Feng, W. Cao, Y. Wang, L. Hong, L. Shen, Z. Mao, Y. Zhu and C. Gao, A Reactive Oxygen Species Scavenging and O 2 Generating Injectable Hydrogel for Myocardial Infarction Treatment In Vivo, *Small*, 2020, **16**(48), 2005038, DOI: **10.1002/smll.202005038.**

39 S. Khanna, A. K. Singh, S. P. Behera and S. Gupta, Thermoresponsive BSA Hydrogels with Phase Tunability, *Mater. Sci. Eng. C*, 2021, **119**, 111590, DOI: **10.1016/j.msec.2020.111590.**

40 G. Navarra, C. Peres, M. Contardi, P. Picone, P. L. San Biagio, M. Di Carlo, D. Giacomazza and V. Militello, Heat- and PH-Induced BSA Conformational Changes, Hydrogel Formation and Application as 3D Cell Scaffold, *Arch. Biochem. Biophys.*, 2016, **606**, 134–142, DOI: **10.1016/j.abb.2016.07.020.**

41 J. Chen, X. Ma, Q. Dong, D. Song, D. Hargrove, S. R. Vora, A. W. K. Ma, X. Lu and Y. Lei, Self-Healing of Thermally-Induced, Biocompatible and Biodegradable Protein Hydrogel, *RSC Adv.*, 2016, **6**(61), 56183–56192, DOI: **10.1039/C6RA11239K.**

42 N. K. Holm, S. K. Jespersen, L. V. Thomassen, T. Y. Wolff, P. Sehgal, L. A. Thomsen, G. Christiansen, C. B. Andersen, A. D. Knudsen and D. E. Otzen, Aggregation and Fibrillation of Bovine Serum Albumin, *Biochim. Biophys. Acta, Proteins Proteomics*, 2007, **1774**(9), 1128–1138, DOI: **10.1016/j.bbapap.2007.06.008.**

43 Y. Moriyama, E. Watanabe, K. Kobayashi, H. Harano, E. Inui and K. Takeda, Secondary Structural Change of Bovine Serum Albumin in Thermal Denaturation up to 130 °C and Protective Effect of Sodium Dodecyl Sulfate on the Change, *J. Phys. Chem. B*, 2008, **112**(51), 16585–16589, DOI: **10.1021/jp8067624.**

44 A. V. Singh, A. Katz, R. S. Maharjan, A. K. Gadicherla, M. H. Richter, J. Heyda, P. del Pino, P. Laux and A. Luch, Coronavirus-Mimicking Nanoparticles (CorNPs) in Artificial Saliva Droplets and Nanoaerosols: Influence of Shape and Environmental Factors on Particokinetics/Particle Aerodynamics, *Sci. Total Environ.*, 2023, **860**, 160503, DOI: **10.1016/j.scitotenv.2022.160503.**

45 M. H. Chen, L. L. Wang, J. J. Chung, Y.-H. Kim, P. Atluri and J. A. Burdick, Methods To Assess Shear-Thinning Hydrogels for Application As Injectable Biomaterials, *ACS Biomater. Sci. Eng.*, 2017, **3**(12), 3146–3160, DOI: **10.1021/acsbiomaterials.7b00734.**

46 B. Yang, Z. Zhao, Y. Pan, J. Xie, B. Zhou, Y. Li, Y. Dong and D. Liu, Shear-Thinning and Designable Responsive Supramolecular DNA Hydrogels Based on Chemically Branched DNA, *ACS Appl. Mater. Interfaces*, 2021, **13**(41), 48414–48422, DOI: **10.1021/acsami.1c15494.**

47 R. S. Maharjan, A. V. Singh, J. Hanif, D. Rosenkranz, R. Haidar, A. Shelar, S. P. Singh, A. Dey, R. Patil, P. Zamboni, P. Laux and A. Luch, Investigation of the Associations between a Nanomaterial's Microrheology and Toxicology, *ACS Omega*, 2022, **7**(16), 13985–13997, DOI: **10.1021/acsomega.2c00472.**

48 C. Yan and D. J. Pochan, Rheological Properties of Peptide-Based Hydrogels for Biomedical and Other Applications, *Chem. Soc. Rev.*, 2010, **39**(9), 3528, DOI: **10.1039/b919449p.**

49 S. De Maria, G. Ferrari and P. Maresca, Rheological Characterization Bovine Serum Albumin Gels Induced by High Hydrostatic Pressure, *Food Nutr. Sci.*, 2015, **06**(09), 770–779, DOI: **10.4236/fns.2015.69080.**

50 X. Ma, X. Sun, D. Hargrove, J. Chen, D. Song, Q. Dong, X. Lu, T.-H. Fan, Y. Fu and Y. ei, A Biocompatible and Biodegradable Protein Hydrogel with Green and Red Autofluorescence: Preparation, Characterization and In Vivo Biodegradation Tracking and Modeling, *Sci. Rep.*, 2016, **6**(1), 19370, DOI: **10.1038/srep19370.**

51 S. T. L. Jales, R. Barbosa, M. de, A. C. de Albuquerque, L. H. V. Duarte, G. R. da Silva, L. M. A. Meirelles, T. M. S. da Silva, A. F. Alves, C. Viseras, F. N. Raffin, T. F. A. Moura and L. de, Development and Characterization of Aloe Vera Mucilaginous-Based Hydrogels for Psoriasis Treatment, *J. Compos. Sci.*, 2022, **6**(8), 231, DOI: **10.3390/jcs6080231.**

52 S. Wei, Z. Li, W. Lu, H. Liu, J. Zhang, T. Chen and B. Z. Tang, Multicolor Fluorescent Polymeric Hydrogels, *Angew. Chem., Int. Ed.*, 2021, **60**(16), 8608–8624, DOI: **10.1002/anie.202007506.**

53 K. Naik, S. Chaudhary, L. Ye and A. S. Parmar, A Strategic Review on Carbon Quantum Dots for Cancer-Diagnostics and Treatment, *Front. Bioeng. Biotechnol.*, 2022, **10**, DOI: **10.3389/fbioe.2022.882100.**

54 P. Li, D. Zhang, Y. Zhang, W. Lu, J. Zhang, W. Wang, Q. He, P. Théato and T. Chen, Aggregation-Caused Quenching-Type Naphthalimide Fluorophores Grafted and Ionized in a 3d Polymeric Hydrogel Network for Highly Fluorescent and Locally Tunable Emission, *ACS Macro Lett.*, 2019, **8**(8), 937–942, DOI: **10.1021/acsmacrolett.9b00337.**

55 Y. Xia, B. Xue, M. Qin, Y. Cao, Y. Li and W. Wang, Printable Fluorescent Hydrogels Based on Self-Assembling Peptides, *Sci. Rep.*, 2017, **7**(1), 1–10, DOI: **10.1038/s41598-017-10162-y.**

56 M. Li, M. Yang, B. Liu, H. Guo, H. Wang, X. Li, L. Wang and T. D. James, Self-Assembling Fluorescent Hydrogel for Highly Efficient Water Purification and Photothermal Conversion, *Chem. Eng. J.*, 2022, **431**, 134245, DOI: **10.1016/j.cej.2021.134245.**

57 F. R. Isfahani, H. Tavanai and M. Morshed, Release of Aloe Vera from Electrospun Aloe Vera-PVA Nanofibrous Pad, *Fibers Polym.*, 2017, **18**(2), 264–271, DOI: **10.1007/s12221-017-6954-9.**

58 A. Upadhyay, R. Kandi and C. P. Rao, Injectable, Self-Healing, and Stress Sustainable Hydrogel of BSA as a Functional

Biocompatible Material for Controlled Drug Delivery in Cancer Cells, *ACS Sustainable Chem. Eng.*, 2018, **6**(3), 3321–3330, DOI: **10.1021/acssuschemeng.7b03485**.

59 F. You, X. Wu, N. Zhu, M. Lei, B. F. Eames and X. Chen, 3D Printing of Porous Cell-Laden Hydrogel Constructs for Potential Applications in Cartilage Tissue Engineering, *ACS Biomater. Sci. Eng.*, 2016, **2**(7), 1200–1210, DOI: **10.1021/acsbiomaterials.6b00258**.

60 A. V. Singh, V. Chandrasekar, P. Laux, P. Luch, S. P. Dakua, P. Zamboni and A. Shelar, Yin Yang Vaibhav Pandit, Veronica Tisato and Donato Gemmati. Micropatterned Neurovascular Interface to Mimic the Blood–Brain Barrier's Neurophysiology and Micromechanical Function: A BBB-on-CHIP Model, *Cells*, 2022, **11**(18), 2801.

61 M. H. D. Ansari, V. Iacovacci, S. Pane, M. Ourak, G. Borghesan, I. Tamadon, E. Vander Poorten and A. Menciassi, 3D Printing of Small-Scale Soft Robots with Programmable Magnetization, *Adv. Funct. Mater.*, 2023, **33**(15), 2211918, DOI: **10.1002/adfm.202211918**.

62 T. Ma, X. Zhai, Y. Huang, M. Zhang, X. Zhao, Y. Du and C. Yan, A Smart Nanoplatform with Photothermal Antibacterial Capability and Antioxidant Activity for Chronic Wound Healing, *Adv. Healthc. Mater.*, 2021, **10**(13), 2100033, DOI: **10.1002/adhm.202100033**.

63 Y. Liang, M. Li, Y. Yang, L. Qiao, H. Xu and B. Guo, PH/Glucose Dual Responsive Metformin Release Hydrogel Dressings with Adhesion and Self-Healing via Dual-Dynamic Bonding for Athletic Diabetic Foot Wound Healing, *ACS Nano*, 2022, **16**(2), 3194–3207, DOI: **10.1021/acsnano.1c11040**.

64 E. H. Kaparakou, C. D. Kanakis, M. Gerogianni, M. Maniati, K. Vekrellis, E. Skotti and P. A. Tarantilis, Quantitative Determination of Aloin, Antioxidant Activity, and Toxicity of Aloe Vera Leaf Gel Products from Greece, *J. Sci. Food Agric.*, 2021, **101**(2), 414–423, DOI: **10.1002/jsfa.10650**.

65 L. A. Dra, S. Sellami, H. Rais, F. Aziz, A. Aghraz, K. Bekkouche, M. Markouk and M. Larhsini, Antidiabetic Potential of Caralluma Europaea against Alloxan-Induced Diabetes in Mice, *Saudi J. Biol. Sci.*, 2019, **26**(6), 1171–1178, DOI: **10.1016/j.sjbs.2018.05.028**.

66 K. Singh, V. B. Yadav, U. Yadav, G. Nath, A. Srivastava, P. Zamboni, P. Kerkar, P. S. Saxena and A. V. Singh, Evaluation of Biogenic Nanosilver-Acticoat for Wound Healing: A Tri-Modal in Silico, in Vitro and in Vivo Study, *Colloids Surf., A*, 2023, **670**, 131575, DOI: **10.1016/j.colsurfa.2023.131575**.

67 K. C. Mbara, S. Rambharose, H. Baijnath, M. Nlooto and P. M. O. Owira, Antidiabetic Effects of Psidium x Durbanensis Baijnath & Ramcharun Ined. (Myrtaceae) Leaf Extract on Streptozotocin-Induced Diabetes in Rats, *J. Ethnopharmacol.*, 2022, **297**, 115542, DOI: **10.1016/j.jep.2022.115542**.

68 N. A. A. Wahab, N. Giribabu, E. K. Kilari and N. Salleh, Abietic Acid Ameliorates Nephropathy Progression via Mitigating Renal Oxidative Stress, Inflammation, Fibrosis and Apoptosis in High Fat Diet and Low Dose Streptozotocin-Induced Diabetic Rats, *Phytomedicine*, 2022, **107**, 154464, DOI: **10.1016/j.phymed.2022.154464**.

69 M. F. Elsadek and B. M. Ahmed, Effect of Sakuranin on Carbohydrate-Metabolizing Enzyme Activity Modifications in Streptozotocin-Nicotinamide-Induced Diabetic Wistar Rats, *Saudi J. Biol. Sci.*, 2022, **29**(3), 1402–1406, DOI: **10.1016/j.sjbs.2021.11.035**.

70 E. Latifi, A. A. Mohammadpour, H. Behrooz Fathi and H. Nourani, Antidiabetic and Antihyperlipidemic Effects of Ethanolic Ferula Assa-Foetida Oleo-Gum-Resin Extract in Streptozotocin-Induced Diabetic Wistar Rats, *Biomed. Pharmacother.*, 2019, **110**, 197–202, DOI: **10.1016/j.biopha.2018.10.152**.

71 H. Raza, S. K. Prabu, A. John and N. G. Avadhani, Impaired Mitochondrial Respiratory Functions and Oxidative Stress in Streptozotocin-Induced Diabetic Rats, *Int. J. Mol. Sci.*, 2011, **12**(5), 3133–3147, DOI: **10.3390/ijms12053133**.

72 E. Zandifar, S. Sohrabi Beheshti, A. Zandifar and S. Haghjooy Javanmard, The Effect of Captopril on Impaired Wound Healing in Experimental Diabetes, *Int. J. Endocrinol.*, 2012, **2012**, 1–6, DOI: **10.1155/2012/785247**.

73 R. Ahmed, R. Augustine, M. Chaudhry, U. A. Akhtar, A. A. Zahid, M. Tariq, M. Falahati, I. S. Ahmad and A. Hasan, Nitric Oxide-Releasing Biomaterials for Promoting Wound Healing in Impaired Diabetic Wounds: State of the Art and Recent Trends, *Biomed. Pharmacother.*, 2022, **149**, 112707, DOI: **10.1016/j.biopha.2022.112707**.

74 A. T. Eprintsev, I. R. Bondareva and N. V. Selivanova, Expression Levels and Activity of Rat Liver Lactate Dehydrogenase Isoenzymes in Alloxan Diabetes, *Biochem. (Moscow), Suppl. Ser. B Biomed. Chem.*, 2022, **16**(3), 210–215, DOI: **10.1134/S1990750822030052**.

75 K.-Y. Cheng, Z.-H. Lin, Y.-P. Cheng, H.-Y. Chiu, N.-L. Yeh, T.-K. Wu and J.-S. Wu, Wound Healing in Streptozotocin-Induced Diabetic Rats Using Atmospheric-Pressure Argon Plasma Jet, *Sci. Rep.*, 2018, **8**(1), 12214, DOI: **10.1038/s41598-018-30597-1**.

76 N. F. Abdul Sani, L. K. Belani, C. Pui Sin, S. N. A. Abdul Rahman, S. Das, T. Zar Chi, S. Makpol and Y. A. M. Yusof, Effect of the Combination of Gelam Honey and Ginger on Oxidative Stress and Metabolic Profile in Streptozotocin-Induced Diabetic Sprague-Dawley Rats, *Biomed Res. Int.*, 2014, **2014**, 1–9, DOI: **10.1155/2014/160695**.

77 F. M. Uckun, C. Orhan, M. Tuzcu, A. S. Durmus, I. H. Ozercan, M. Volk and K. Sahin, RJX Improves Wound Healing in Diabetic Rats, *Front. Endocrinol. (Lausanne)*, 2022, 13, DOI: **10.3389/fendo.2022.874291**.